Title
The deformation and fracture of human cortical bone across multiple length-scales

Author
Zimmermann, Elizabeth Ann

Publication Date
2011

Peer reviewed|Thesis/dissertation

Deformation and fracture of human cortical bone across multiple length-scales

by

Elizabeth Ann Zimmermann

A dissertation submitted in partial satisfaction of the

requirements for the degree of

Doctor of Philosophy

In

Engineering – Materials Science and Engineering

in the

Graduate Division

of the

University of California, Berkeley

Committee in charge:

Professor Robert O. Ritchie, Chair
Professor Andrew Minor
Professor Lisa A. Pruitt

Fall 2011

Abstract

The deformation and fracture of human cortical bone across multiple length-scales

by
Elizabeth Ann Zimmermann
Doctor of Philosophy in Materials Science and Engineering
University of California, Berkeley
Professor Robert O. Ritchie, Chair

The complex structure of human cortical bone evolves over multiple length-scales from its basic constituents of collagen molecules and hydroxyapatite crystals at the nanoscale to the osteonal structures at near-millimeter dimensions. There is a need to understand how all levels of the structure contribute to the deformation and fracture resistance of cortical bone under physiological loading conditions and how structural changes due to aging and disease lead to diminished mechanical properties. The first part of this thesis addresses the latter by using non-enzymatic crosslinking measurements and *in situ* small- and wide-angle x-ray scattering/diffraction to characterize changes in the bone structure at sub-micron dimensions, while synchrotron x-ray computed micro-tomography and *in situ* fracture-toughness measurements in the scanning electron microscope were performed to characterize corresponding changes at micron-scale dimensions. This multi-scale analysis allows us to better understand how load is transferred across multiple length-scales and how biological aging impacts energy absorption throughout the structure. The second part of this thesis addresses the fracture toughness of human cortical bone under multiaxial loading. Most studies to date have only considered the toughness of bone under mode I (tensile) loading conditions; however, due to the complex, anisotropic structure of cortical bone, the mode I fracture toughness is not necessarily the limiting value. Thus, this research investigates the effects of combined tensile and shear loading at the crack tip on the initiation and crack-growth toughnesses to better understand how bone fractures under physiologically relevant loading conditions.

Table of Contents

Acknowledgements

First, I would like to thank Professor Robert O. Ritchie for mentoring me over the past five years. Prof. Ritchie is a model of academic excellence, be it through the care and time he devotes to teaching, or the breadth and depth of his knowledge/research; I feel truly honored to have worked with him.

Many thanks are also due to Dr. Joel W. Ager III for pushing me to be a creative researcher. I also thank Dr. Tony Tomsia and the many students, past and present, that I have the pleasure of working with; however, I owe special thanks to Drs. Maximilien Launey and Bjorn Busse for devoting extra time to my development as a researcher.

This research has required extensive use of the Advanced Light Source, which would not have been possible without the scientific expertise of Dr. Alex Hexemer, Eric Schaible, Peter Reichert, and Steven Alvarez at beamline 7.3.3 as well as Dr. Alastair MacDowell at beamline 8.3.2. I am also indebted to my fellow group members Holly D. Barth and Dr. Hrishikesh Bale for spending countless hours at the beamline with or without me.

I would like to thank Drs. Tamara Alliston and Simon Y. Tang at the University of California San Francisco for their help with crosslinking measurements as well as Dr. Tony M. Keaveny and Mike Jekir at the University of California, Berkeley for use of their facilities and as a source of cortical bone. I would like to thank my thesis committee for providing academic support.

Lastly, thank you to my family and friends back home in Chicago for supporting my decision to pursue my PhD at Berkeley as well as my friends in California for their camaraderie throughout grad school.

This work was supported by the National Institute of Health (NIH/NIDCR) under grant no. 5R01 DE015633 to the Lawrence Berkeley National Laboratory (LBNL) and the Laboratory Directed Research and Development Program of LBNL funded by the U.S. Department of Energy under contract no. DE-AC02-05CH11231.

List of figures

deflection and twist divert the crack tip from the direction of maximum driving force; this potent source of toughening occurs in the transverse orientation.

Fig. 3.1 The tension tests on both *Young* and *Aged* bone were performed with a custom built tension rig that applied displacement to the sample. Using a procedure similar to Gupta et al. [46], the samples were exposed to high-flux x-ray radiation causing the 67-nm stagger in the mineralized collagen fibril to diffract x-rays at a small angle (*i.e.*, SAXS) and the lattice of the hydroxyapatite crystals to diffract x-rays at a high angle (*i.e.*, WAXD). As load was applied to the bone, changes in the peak positions were used to calculate the mineral and fibril strains, while the tissue strain was measured with a CCD camera (not pictured).

Fig. 3.2 *In vitro* mechanical properties of human cortical bone in 25°C HBSS as a function of aging showing (a) strength and (b) fracture toughness R-curve properties for the *Young* (34 – 41 years old), *Middle-Aged* (61 – 69 years old), and *Aged* (85 – 99 years old) groups. The R-curve results encompass (long crack growth) data, measured using crack sizes from ~500 μm to several mm from ref. [36], in addition to the current results on realistically short cracks (< 500 μm) extensions performed *in situ* in the ESEM. The inset schematics describe the orientation of the osteons with respect to the sample geometry.

Fig. 3.3 (a, b) X-ray computed micro-tomography of *Young* and *Aged* bone samples show three-dimensional images of the crack profile after roughly 500 μm of crack growth from a razor-sharpened notch (white arrows). (c, d) SEM images during small-crack R-curve experiments confirm the presence and absence of crack bridging (other arrows) in the *Young* and *Aged* bone, respectively.

Fig. 3.4 X-ray computed micro-tomography was also used to image the size and density of Haversian canals in the (a) *Young* and (b) *Aged* human cortical bone. The color coding in (a,b) indicates the diameter of the Haversian canals. (c) As is strikingly apparent from the three-dimensional images, in terms of osteonal density (On.Dn.), the *Aged* bone has nearly three times the osteonal density than the *Young* bone. A higher volume of osteons implies more cement lines for microcracks to initiate and smaller crack bridges during crack growth.

Fig. 3.5 The results of the (a) small- and (b) wide-angle x-ray scattering/diffraction experiments for tensile testing of *Young* and *Aged* cortical bone samples in the longitudinal orientation. For each individual tensile test, the strain values were binned every 0.1% tissue strain for the SAXS and WAXD experiments, respectively. For each age group, the average and standard deviation of the binned values from the tensile tests were calculated and are shown as the dots and error bars, respectively. Inset (c) shows a representative stress-strain curve for the tensile tests. (d) At a fixed tissue strain, the individual strain in the fibrils is ~25% smaller in the *Aged* bone than *Young* bone, while changes in the mineral strain are not significant.

Fig. 3.6 The accumulation of advanced glycation end-products (AGEs) was fluorimetrically quantified in the cortex of the humeri in the *Young* and *Aged* bone samples. AGEs increase significantly with biological aging, with the *Aged* bone containing nearly three times as many fluorescent crosslinks as the *Young* bone. AGEs result from the reactive non-enzymatic glycation between amino residues and sugars that increases crosslinking in collagen.

Fig. 4.1 Schematic illustrating the different modes of loading: (a) mode I (tensile loading), (b) mode II (shear loading), and (c) mixed mode. Mixed-mode loading is a superposition of the mode I and mode II stress intensities that creates a mixed-mode driving force at the crack tip; in this case, cracks are expected to grow at an angle, θ, to the original crack plane.

Fig. 4.2 The typical relationship between the critical strain energy release rate, G_c, and the phase angle, Ψ, for a variety of materials, namely wood (in its longitudinal direction) [97], alumina [83], and zirconia [83]. For comparison, G_c is here normalized by the lower-bound toughness, G_o. The toughness is lowest in mode I, at $\Psi = 0°$, and increases monotonically with the relative proportion of the mode II shear component until reaching a maximum under mode II conditions, at $\Psi = 90°$.

Fig. 4.3 The single-edge notched specimens were tested using an asymmetric four-point bend rig. The load is applied through the center line of the rig, which creates, through the mid-span of the sample, a constant shear force and a linearly varying bending moment. Vertical lines 1 and 4 represent the location of the inner loading pins. When the crack is aligned with the centerline of the rig, line 3, only a shear force is applied, which creates a mode II driving force. When the crack is offset from the centerline of the

rig, for example line 2, a shear force and a moment are applied which creates a mixed-mode driving force. Thus, the phase angle, defined as $\Psi = \tan^{-1}(K_{II}/K_I)$, is a function of the offset of the crack, *c*, from the centerline.

Fig. 4.4 The critical strain energy release rate, G_C, as a function of the phase angle, Ψ, is plotted for human cortical bone in the (a) transverse orientation and (b) the longitudinal orientation. The phase angle signifies the relative proportion of K_{II} to K_I; thus, for pure mode I tensile loading $\Psi = 0°$, while for pure mode II shear loading $\Psi = 90°$. While in the longitudinal orientation bone is strong in shear, the trend reverses in the transverse direction. This unique result sheds light on the strong influence of the microstructural orientation as compared to the applied mechanical driving force. In the insets, the dark brown lines indicate the direction of the weak microstructural planes, while the pink arrows indicate the direction of the maximum mechanical applied driving force (*i.e.*, G_{max} or $K_{II}=0$), which in mode I is coplanar with the original crack plane and in mode II is at about a 74° angle to the original crack plane [86]. Thus, a high toughness results when the driving force is perpendicular to the weak planes (transverse mode I and longitudinal mode II). As the preferred mechanical and microstructural directions get closer to alignment, the toughness correspondingly decreases. **The longitudinal data represent a lower-bound for the expected values and are compared to data from Norman *et al*. [91].

Fig. 4.5 Environmental scanning electron microscope (ESEM) backscattered-electron images of stable crack growth during *in situ* testing in the transverse orientation for phase angles of (b) $\Psi = 0°$, (c) $\Psi = 12°$, (d) $\Psi = 25°$, (e) $\Psi = 52°$, and (f) $\Psi = 90°$. (a) The crack growth angle, θ, (in green), with respect to the original crack plane (in red), increases with the phase angle. The direction of maximum driving force (in blue) is also indicated and is defined here as the G_{max} path [86]. In (b-f), the scale bars are 50 μm.

Fig. 4.6 Experimental crack deflection angle, θ, as a function of phase angle, Ψ, for human cortical bone in the transverse orientation, silica glass [98], and alumina [83]. The green line indicates the predicted angle of deflection as a function of phase angle for a material following the maximum driving force condition, G_{max}, [86] while the orange line indicates the position of the weak planes in this geometry. Traditional brittle materials follow the maximum driving force condition when a mixed-mode load is applied. However, application of a shear force in addition to the tensile force causes the direction of the driving force to change such that deflection along the weak microstructural planes becomes increasingly promoted.

Fig. 4.7 SEM fractography images of human cortical bone after *in situ* testing in the transverse orientations for phase angles of (a) $\Psi = 0°$ and (b) $\Psi = 90°$. The mode I sample shows a torturous crack path due to the disparity between the orientation of the driving force and the weak microstructural path; this toughens the material. The mode II sample shows a macroscopic inclination of the crack, on the order of millimeters, which is promoted by the alignment of the driving force and the weak planes; this contributes little to the toughness of the material. In (a) and (b), the scale bars are 1 mm.

Fig. 4.8 X-ray computed micro-tomography images of human cortical bone after *in situ* testing in the transverse orientation for phase angles of (a,c) $\Psi = 0°$ and (b,d) $\Psi = 72°$. In (a) and (b), the notch is colored white, the crack growth is in blue, and the Haversian canals are yellow. (a) The three-dimensional image of the mode I sample shows nominally straight crack growth with a deflection as the crack approaches a Haversian canal while the high phase angle sample (b) shows one large deflection. Images (c) and (d) are the crack paths from the back-face of the sample, *i.e.*, the crack is growing into the image. Both the high phase angle sample and the mode I sample, exhibit crack bridging and twisting. The arrows point to areas of high-angle twisting.

Fig. 5.1 (a) A magnified view of the crack tip shows that when the crack deflects with respect to the original plane of the crack, local stress intensities (k_1 and k_2) arise at the crack tip; the local k's are derived from the global stress intensities (K_I and K_{II}) via a kinked-crack solution. The global stress intensities are calculated with the asymmetric four-point bend solution for a crack with length $a = a_o + \Delta a_p$, which is the length of the kinked crack projected onto the original crack plane. (b) When an asymmetric load is applied, the crack deflects at an angle θ from the original crack plane. The direction of the G_{max} path at each increment of crack growth is assessed from the local stress intensities using the analysis of He and Hutchinson [86].

Fig. 5.2 Traditional two-dimensional R-curves for human cortical bone in the transverse orientation loaded in (a) mode I ($\Psi = 0°$), (b) at low phase angles ($\Psi = 12\text{-}25°$), and (c) at high phase angles ($\Psi = 55\text{-}90°$). The resistance of the material is measured in terms of the strain energy release rate and given as a function of crack extension. As previous R-curves for the tensile opening case have shown, bone exhibits stable crack extension in combined mode I-II loading [34]. The occurrence of a rising R-curve thus indicates that as the crack grows, a larger driving force is needed for crack extension. At higher phase angles, the R-curve is shallower because the paths of maximum mechanical driving force and the preferred microstructural paths (generally along the cement lines) are

more closely aligned, which encourages crack deflection along the brittle interfaces in the microstructure.

Fig. 5.3 Three-dimensional R-curves for transverse-orientated human cortical bone obtained by plotting the two-dimensional R-curves from Fig. 5.2 together with an additional axis that represents the phase angle, Ψ. The marked decrease in the fracture resistance of the material with crack growth can be seen as the amount of mode II loading (phase angle) increases. The dotted lines are the projections of the three-dimensional lines onto the Ψ-Δa axis.

Fig. 5.4 Two-dimensional R-curves for the (a) mode I, (b) mixed-mode, and (c) mode II samples of transverse-orientated human cortical bone along with an image of the crack extension. The dotted red line indicates the initial crack position, the dotted blue lines indicate the increments of crack growth, and the orange lines indicate the G_{max} direction. With respect to the comparison between the G_{max} direction and the actual crack path, higher toughness values result when the driving force is perpendicular to the weak microstructural path.

Fig. 5.5 Crack bridging in human cortical bone for a crack loaded in shear (mode II). The crack follows the preferred microstructural path, which is perpendicular to the original plane of the crack. Such apparent shear cracks propagate in a fashion very similar to *en echelon* cracks associated with earthquake faults in microcracking rocks.

Chapter 1: Introduction

Aging and disease cause detrimental changes to the quantity and quality of bone leading to an increased risk of fracture. With an aging population, this is of particular concern due to the economic impacts of, and quality of life after, a fracture. As bone is continuously adapting to its environment, the increased fracture risk is mainly due to changes in the structure induced by biological or mechanical stimuli. A major influence on the fracture risk (especially in the case of aging and osteoporosis) is a loss in bone mass or bone-mineral density: an issue of *bone quantity*. However, recent studies have shown that the structure and properties (*i.e.,* mechanical properties, rate of turnover, microdamage accumulation, and geometry) specifically degrade with aging and disease [1, 2]: an issue of *bone quality.* The toughness of bone, or its ability to resist fracture, is a critical characteristic of bone quality [3]. Thus, over the past two decades, there has been much interest in understanding how bone fractures so that better treatments to combat aging and disease may be developed.

Another interesting application of bone-related research is for the design and engineering of new materials. Cortical bone and other biological materials (*e.g.,* nacre, dentin, antler, etc.) have a unique combination of strength and toughness. These properties have evolved to suit the material's particular loading environment through Nature's engineering of a hierarchical structure. Understanding how energy is absorbed through this structure will not only improve treatments for diseased bone but also aid in the design of novel engineering materials and replacements for bone.

Indeed, the hierarchical structure of cortical bone evolves over numerous length-scales leading to a complex mechanical response, with contributions from each level of the structure. The smaller length-scales, those at the collagen and mineral level, deform via mechanisms that impart strength to the material, while microstructural mechanisms at the higher levels of the hierarchy, *i.e.,* osteons and lamellae, impart toughness. The degree to which the mechanisms at each length-scale actively absorb energy during deformation is particularly important in shaping the mechanical properties of bone.

Because cortical bone's mechanical properties are known to deteriorate with age, the first part of this thesis examines how various age-related biological changes at different length-scales affect the intrinsic and extrinsic fracture resistance. To do this, the deformation and fracture mechanisms will be analyzed experimentally at various length-scales on a set of bones from different age groups. Advanced glycation end-product measurements (*i.e.,* degree of crosslinking) in conjunction with *in situ* x-ray scattering experiments will characterize changes at the level of the mineralized collagen fibril, while mechanical tests of both the strength and toughness followed by x-ray computed micro-tomography will reveal mechanical and structural changes at higher hierarchical levels.

The second part of this thesis focuses on how bone fractures under multiaxial loading. Indeed, bone is routinely loaded multiaxially *in vivo* with combinations of tension, shear, and torsion producing mode I, II, and III stress intensities at pre-existing cracks. In the literature, the toughness of bone has been predominately characterized under tensile mode I conditions. However, due to its complicated structure, the mode I toughness is not necessarily the limiting value and the mechanisms of crack growth under mixed-mode conditions may be different. Thus, this thesis provides insight into how the anisotropic structure imparts toughness to bone under multiaxial loading conditions.

Chapter 2: Background

Bone is a composite of collagen and hydroxyapatite (HA), with characteristic structural features over innumerable length-scales ranging from collagen molecules and hydroxyapatite crystals at the nanoscale, to osteon structures at the scale of hundreds of microns. The unique mechanical properties of human cortical bone, that of stiffness (~15-25 GPa), strength (~100 MPa), and toughness (≥ 5 MPa/m)[1], are a direct result of the various deformation and fracture mechanisms that occur at each level of its hierarchical structure.

2.1. Structure of cortical bone

At its smallest length-scale, bone is composed of collagen molecules mineralized with HA nanoplatelets. The roughly 150-nm-long collagen molecules individually consist of three polypeptide chains arranged in a triple helix, which is stabilized by hydrogen bonding between residues [4-6]. The collagen molecules form an array with a 67-nm stagger (see Fig. 2.1) [7]; the formation of this array is hypothesized to be stabilized by immature enzymatic crosslinks between the collagen molecules [8]. These crosslinks form due to an enzyme-mediated reaction between lysine residues in the telopeptide region (*i.e.*, the unwound portion at the ends of the molecules) and helical hydroxylysine residues of neighboring molecules [9]. Immature crosslinking is predominately found in young bone tissue [10], where the ketoamine hydroxylysino-ketonorleucine (HLKNL) is the predominant immature enzymatic crosslink.

Mineralization of the collagen array gives an otherwise weak structure greater strength. The HA nanocrystals (roughly 50 nm in both length and width as well as 5 nm in thickness [11]) are deposited first in the gaps between the heads and tails of the collagen molecules [12, 13] followed by the overlap zone of the collagen array (*i.e.*, along the 67-nm stagger) and also extrafibrillarly on the surface of the fibril [14-16]. It is important to note that the c-axis of the hexagonal HA crystals deposited within the gaps and overlap zones is aligned with the collagen molecules [11]; this periodicity within the structure allows the strain in the mineral and the fibril to be measured at this length-scale via x-ray diffraction. Together this structure composed of collagen and mineral is called a mineralized collagen fibril and forms the basic building block of many biological materials (from tendons and skin to hard mineralized tissues such as bone), see Fig. 2.1.

[1] Stiffness is related to the elastic modulus and defines the force required to produce corresponding elastic deformation. Strength, defined by the yield stress at the onset of permanent deformation or maximum strength at the peak load before fracture, is a measure of the force/unit area that the bone can withstand. The fracture toughness measures the resistance to fracture of a material.

At the fibril level, two predominant forms of crosslinks exist in collagenous tissues: enzymatic and non-enzymatic advanced glycation end-products (AGEs). The amount of immature enzymatic crosslinks that originally stabilize the quarter stagger of collagen molecules begins to decrease until reaching a plateau around 15 years of age [10]. During this period, the immature crosslinks are believed to undergo modifications to produce stable non-reducible crosslinks [9], such as hydroxylysyl-pyridinoline (pyr) and pyrroles in bone. The mature crosslinks predominately form interfibrillarly (*i.e.*, between collagen molecules in neighboring fibrils). Non-enzymatic AGEs are produced due to a reaction between the collagen molecules and glucose. These crosslinks form inter- and intrafibrillarly and dramatically increase with aging and disease (such as diabetes) [17].

Arrays of mineralized collagen fibrils form the next structural level termed fibers, while arrays of fibers form 3- to 7-μm-thick sheets termed lamellae [18]. Lamellae concentrically surround a central vascular channel called the Haversian canal[2]; together, this 250- to 300-μm-diameter structure is called a secondary osteon (see Fig. 2.1). The term 'secondary' derives from the fact that bone remodels (*i.e.*, an osteon is resorbed due to damage etc. and then replaced). Secondary osteons contain a roughly 5-μm-thick hypermineralized [21] outer layer called the cement line, which is deposited prior to the osteon's lamellae and delimits the new osteon from the interstitial lamellae [22, 23]. The cement line, not present in primary osteons, represents an especially weak region, which can act as a site where major microcracks form. The secondary osteons in bone, and thus the cement lines, are deposited such that they are aligned with the long axis of the long bones (see Fig. 2.1); this fact is responsible for the anisotropic mechanical properties of cortical bone when tested perpendicular and parallel to the osteons.

Noncollagenous proteins and water are also found in cortical bone. The noncollagenous proteins include osteopontin, osteocalcin, and bone salioprotein. Osteopontin is primarily found at the many boundaries present in the bone structure, including between neighboring fibrils and lamellae, in cement lines, and at the bone's boundary with implants [24]. While playing a large role in regulating the growth of hydroxyapatite crystals and structural formation in bone, osteopontin may also act as a 'glue' between these interfaces during deformation, a so called 'hidden' length-scale [24-26].

The hierarchical structure of human cortical bone has evolved to suit its function as the load bearing entity in the human body. The complex, anisotropic structure, which develops over many length-scales, endows the bone with its unique combination of strength and toughness.

[2] In successive sheets of lamellae, the orientation of the collagen fibers is slightly tilted with respect to the neighboring lamellae; the orientation of the fibers changes by about 10-20° in successive lamellae [19, 20].

2.2. Fracture of bone

The anisotropic structure of human cortical bone has evolved primarily to support loading along the axis of the long bones: strength values are roughly 120 MPa [27] when loaded along the longitudinal direction and roughly half that in both the radial and circumferential directions (see Fig. 2.2). Additionally, as the weak cement lines are nominally aligned with the long axis of the bone, the toughness is roughly 1.5 times higher in the transverse orientation compared to the longitudinal orientation (see Fig. 2.2) [28].

The fracture toughness of bone has been measured on notched samples via linear elastic fracture mechanics (LEFM), which uses the critical stress intensity factor, K_c, or the critical value of the strain energy release rate, G_c, to characterize the toughness [28-32]. An essential assumption of LEFM is that the material is linear elastic; thus, the region within the material experiencing inelastic deformation[3] must be small. This region is called the plastic zone and its size, r_y, can be estimated by the following equation:

$$r_y = \frac{1}{2\pi}\left(\frac{K_I}{\sigma_Y}\right)^2$$

where σ_y is the yield stress. If the plastic zone size is at least one order of magnitude smaller than both the in-plane dimensions (*i.e.*, the crack length, a, and the width, W, see Fig. 2.2) and the out-of-plane dimension (*i.e.*, the thickness, B), then a condition of small-scale yielding exists due to K-field dominance and plane-strain conditions, respectively.

The stress intensity factor, K, characterizes the stress or displacement field at the crack tip in terms of the global parameters and takes the following form:

$$K = Q\sigma_{app}\left(\pi a\right)^{1/2}$$

where Q is a dimensionless factor that depends on the sample geometry, σ_{app} is the applied stress, and a is the crack length. The critical value of the stress intensity, K_c, represents the beginning of unstable fracture, which usually occurs at the peak stress [33]. Assuming linear elasticity, the strain energy release rate is an equivalent energy-based method, where G can be expressed in terms of K as follows:

$$G = \frac{K_I^2}{E'} + \frac{K_{II}^2}{E'} + \frac{K_{III}^2}{2\mu}$$

where K_I, K_{II}, and K_{III} are the mode I, II, and III stress intensity factors, respectively; E′ is the elastic modulus in plane stress ($E' = E$) or $E' = E/(1-\nu^2)$ in plane strain, where E is the elastic modulus and υ is Poisson's ratio); and μ is the shear modulus. The strain energy

[3] Inelastic deformation may occur due to non-recoverable plasticity mechanisms at various length-scales (*e.g.*, molecular uncoiling, fibrillar sliding, and microcracking) within bone, which will be discussed in the following section.

release rate is essentially the change in potential energy for an increment of crack extension.

It is important to note that in some cases, the condition for small-scale yielding may not be satisfied (*i.e.*, the plastic zone size is on the same scale as the sample dimensions). In this case, an approach using nonlinear-elastic fracture mechanics, called the J-integral, must be used [33]. This approach more accurately captures the stress field at the crack tip as well as the contribution from plastic deformation prior to, and during, crack extension. In bone, the J-integral is commonly needed to measure the toughness in the transverse orientation, where the plastic zone size is large due to crack deflections [34, 35].

K_c, G_c, and J_c all provide a single-value measure of the toughness; however, in materials such as bone that permit stable crack extension, a single value of the toughness is insufficient to completely characterize the material's fracture resistance. In this case, it is necessary to measure the toughness (via K, G, or J) as a function of crack extension with a crack-growth resistance curve (R-curve). This can be done by calculating the stress intensity at each increment of crack extension as monitored during testing via imaging (*e.g.,* optical or scanning electron microscopy) or compliance-based measurements [33]. Cortical bone has been shown to have a rising R-curve, which implies that the driving force needed for crack extension increases as the crack grows [34-37]. For this reason, bone can support a density of microcracks and in turn, use microcracking to signal remodeling.

Rising R-curve behavior occurs due to crack-tip shielding mechanisms that are activated by crack growth. The mechanisms, by means of carrying load or applying a compressive stress to the crack tip, shield the crack from the full applied stress intensity [38]. The next section will elaborate on how the structure of cortical bone is able to absorb energy or shield the crack as load is transferred through each level of the hierarchy.

2.3. Intrinsic toughness

Intrinsic toughness describes a material's inherent ability to resist fracture, *i.e.*, to inhibit both the initiation and growth of cracks. Intrinsic toughening mechanisms operate ahead of a growing crack and in bone can be identified with plasticity (strictly inelasticity) mechanisms that are derived primarily at sub-micrometer length-scales [39]. Most plastic deformation mechanisms in bone are accommodated at these smallest dimensions; the smallest levels provide strength, while larger length-scales govern toughness [40, 41].

At the smallest length-scale, bone deforms by stretching and unwinding of individual collagen molecules and by deformation in the mineral's crystalline lattice. The polymeric nature of the collagen molecules allows them to uncoil and slide with respect to other collagen molecules by first entropic (untangling of the collagen

molecule) and then energetic mechanisms (uncurling of the triple helix and breaking of the hydrogen bonds) [42, 43]. The nanoscale dimensions of the HA nanocrystals make them flaw tolerant (*i.e.*, imperfect crystals have the theoretical strength of a perfect crystal due to their size); thus, lattice vacancies, substitutions or other flaws in the crystal structure, which cause atomically sharp cracks, will not lead to failure in individual crystals [44]. Flaw tolerance in HA occurs when the thickness of the crystal is roughly below 30 nm; in bone, the HA crystals are only a few nanometers thick.

At the next length-scale, the mechanical properties of the mineralized collagen fibril reflect the composite deformation of the collagen and HA, giving bone its unique combination of strength and toughness. The shear lag model describes how load is transferred between each component in the fibril [45]. Essentially, within the fibril, the mineral carries a tensile load, which is distributed between mineral platelets via a shear force in the collagen molecules. This model correlates with the strain ratios (*i.e.*, tissue:fibril:mineral) measured in bovine bone tissue using small- and wide-angle x-ray scattering/diffraction with simultaneous mechanical tests [46]. In this study, Gupta *et al.* identified fibrillar sliding to be the main deformation mechanism responsible for plasticity at this level. The effectiveness of fibrillar sliding in turn depends on structural aspects of the mineralized collagen fibril, such as the mineral/collagen interface [47-49], inter- and intrafibrillar crosslinking [9, 50, 51], and sacrificial bonding [25, 52, 53] due to noncollagenous proteins at the fibrillar interface. This mechanism of load transfer between the collagen molecules and HA platelets within a fibril enables a large regime of dissipative deformation once plastic yielding begins in mineralized tissues [46, 54, 55] and other biological materials [56]. The molecular behavior of the protein and mineral phases (fibrillar sliding) during large-scale deformation of the mineralized collagen fibrils represents the principal mechanism of plasticity at this length-scale. As in most materials, plasticity provides a major contribution to the intrinsic toughness by dissipating energy and through the formation of "plastic zones" surrounding incipient cracks that further serve to blunt crack tips, thereby reducing the driving force (*i.e.*, stress intensity) for crack propagation.

This notion of sacrificial bonding also exists within higher levels of the bone's structure. The 'glue' provided by the noncollagenous proteins not only connects neighboring fibrils, fibers, and lamellae but also plays a mechanical role by allowing bonds to break and reform. Thus, shearing and stretching of the interfibrillar matrix and between fibrils occurs absorbing energy [46, 52, 57].

Additionally, the process of microcracking can act as a plasticity mechanism by dissipating energy at coarser length-scales typically exceeding several micrometers [58]. Microcracking may also signal remodeling by severing the connections between osteocytes [3].

2.4. Extrinsic toughness

Extrinsic toughening mechanisms act primarily in the wake of a growing crack to "shield" it from the applied stresses; their potency in resisting the growth of cracks depends on the size of the crack. In bone, they can be identified by the mechanisms of crack deflection/twist and bridging [34, 59], and are created principally by the interaction of growing cracks with the osteon structures. As such, they are derived at much larger length-scales in the range of 10-100s μm.

Crack deflection, the most potent extrinsic toughening mechanism, occurs when the growing crack deviates from its original trajectory (see Fig. 2.3). The stress intensity at the deflected crack tip will then have a combination of tensile and in-plane shear components, which can reduce the stress intensity at the crack tip by half for a deflection of 90° [60]. Thus, the toughness increases when cracks deflect because a larger applied driving force is needed for an additional increment of crack extension. A similar effect occurs when the crack twists, except now there will be an additional out-of-plane shear component at the crack tip. Several structural features, such as osteocyte lacunae, porosity, etc., can lead to deflection of the crack path. But it is the largest features, specifically the secondary osteons, that are the most effective at deflecting cracks. Their key feature is the osteonal boundaries, the cement lines, which as hyper-mineralized regions act as the primary location for microcracking. As the osteons are aligned nominally along the long axis of the bone, the microcracks are also largely oriented in this direction [61]. Crack deflection is the primary toughening mechanism for cracking in the transverse (breaking) orientation, where these microcracks are aligned roughly perpendicular to the path of the main crack.

Crack bridging occurs when material spans the crack wake (*i.e.*, uncracked ligaments or collagen fibers) and carries a portion of the applied load thus shielding the crack tip from the full stress intensity (see Fig. 2.3). Crack bridging is the main toughening mechanism in the longitudinal orientation because in this orientation, microcracks form parallel or ahead of the main growing crack. Estimates of the contribution of crack bridging to the toughness using bridging models found that larger bridges provide a more significant contribution to the toughness than collagen fiber bridges [58].

Constrained microcracking can also be considered an extrinsic toughening mechanism. When microcracks occur during crack growth, they open and as a result apply a compressive force to the crack tip (see Fig. 2.3), which shields it. While microcracking does not significantly contribute to the toughness [58], bone's ability to microcrack does enable the main toughening mechanisms of crack deflection and crack bridging.

2.5. Figures

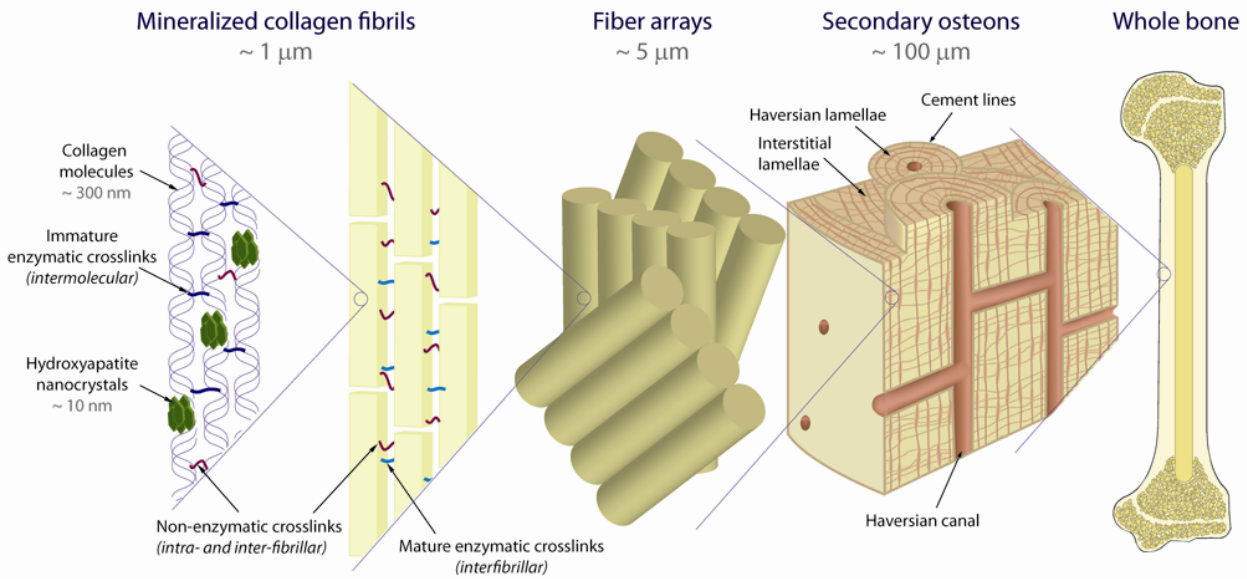

Fig. 2.1 Each level of the hierarchical structure is involved in the deformation and fracture of human cortical bone; the smaller levels add to the intrinsic toughness via plasticity mechanisms, while the higher length-scales contribute to the extrinsic toughness via crack-tip shielding mechanisms. At the nanoscale, molecular uncoiling of collagen molecules occurs as well as fibrillar sliding [46], which is essentially shearing of the organic phase between the mineral particles. Crosslinks form at these length-scales between the collagen molecules and between the fibrils [9]. At higher structural levels, microcracking absorbs energy, while signaling the initiation of bone remodeling. At the microstructural level, the weak boundaries in the secondary osteon's structure (*e.g.*, cement lines, lacuna-canalicular channels) absorb energy by microcracking during crack growth to toughen the structure mainly via crack bridging, crack deflection, and crack twisting [34, 62]. In long bones, such as femora and humeri, the osteons are nominally aligned with the long axis of the bone, which endows anisotropy to cortical bone's mechanical properties.

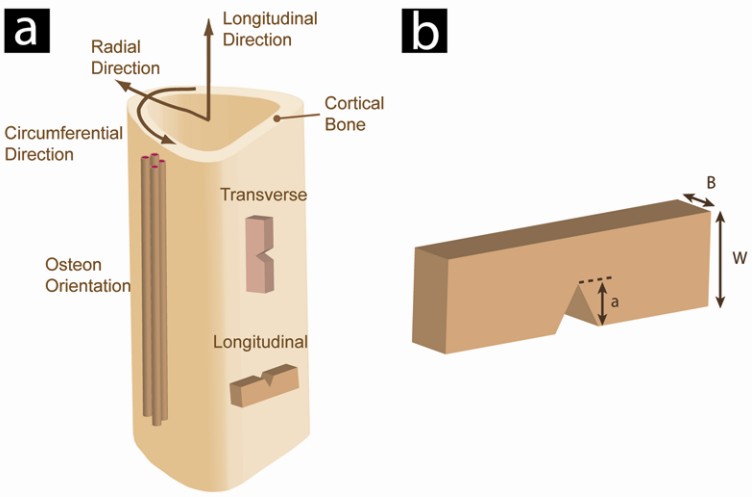

Fig. 2.2 (a) Cortical bone is predominantly found in the diaphysis of long bones (*e.g.*, the humerus, tibia, and femur), where the osteons are nominally aligned with the long axis of the bone, which is called the longitudinal direction. Fracture experiments are performed with notched samples; therefore, it is necessary to specify the direction of crack growth with respect to the microstructure. In the case of the longitudinal orientation, the crack plane is perpendicular to the circumferential direction and crack growth occurs in the longitudinal direction. In the transverse orientation, the crack plane is perpendicular to the longitudinal direction and crack growth occurs in either the radial (see the transverse inset) or circumferential direction (not pictured). Inset (b) depicts a typical fracture toughness sample, showing the crack length, a, the width, W, and the thickness, B.

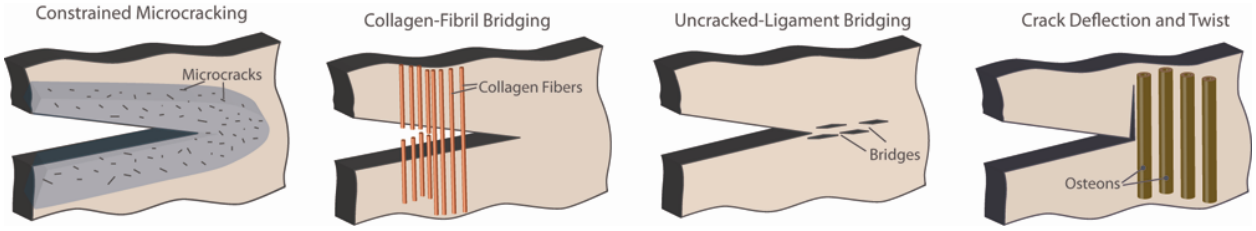

Fig. 2.3 Bone's extrinsic toughness (*i.e.*, resistance to crack propagation) derives primarily from four crack-tip shielding mechanisms acting in the wake of the crack. Constrained microcracking, where the dilation of microcracks applies a compressive stress to the crack tip, and collagen fibril bridging both provide small contributions to the toughness [58]. Uncracked-ligament bridges occur when uncracked material spanning the crack wake carries load, which would otherwise be used to drive the crack; this is the main source of toughening in the longitudinal orientation [36]. Crack deflection and twist divert the crack tip from the direction of maximum driving force; this potent source of toughening occurs in the transverse orientation.

Chapter 3: Age-related changes in the plasticity and toughness of human cortical bone at multiple length-scales

3.

3.1. Introduction

Human cortical bone is a nanocomposite of collagen molecules and nanocrystals of hydroxyapatite (HA) mineral. However, its essential mechanical properties, that of stiffness (~15-25 GPa), strength (~100 MPa), and toughness (≥ 5 MPa/m), are not derived solely from the characteristic structure at the nanoscale but rather at multiple length-scales through bone's hierarchical architecture, which extends from molecular dimensions to the Haversian (osteon) microstructures at near-millimeter levels. Indeed, salient mechanisms that strengthen and toughen bone can be identified at most of these length-scales (Fig. 2.1 and 2.3) and can be usefully classified, as in many materials, in terms of intrinsic and extrinsic toughening mechanisms acting ahead and behind the crack tip, respectively, to absorb energy during crack initiation and growth.

Aging is known to markedly increase the risk of fracture in bone, particularly in post-menopausal women. Although a major reason for this is the age-related loss in bone mass or bone-mineral density (an issue of *bone quantity*), in recent years several studies have additionally shown that the structure and properties of the bone specifically degrade with age (an issue of *bone quality*). This was brought to the fore in a study by Hui *et al*. [2] that showed a ten-fold increase in fracture risk with aging that was independent of the bone mineral density. Several studies have now shown a deterioration in the bone toughness with age [29, 62], presumably as a result of aging-related nano- to micro-structural changes. These changes include progressively larger osteonal dimensions and densities [27], increased non-enzymatic crosslink densities [63], and increased microcracking [61]. Of importance here are the increased collagen crosslinking and osteonal dimensions. In human cortical bone, the former occurs in two forms: i) enzymatic crosslinks occur as immature intrafibrillar crosslinks (DHLNL and HLNL) as well as mature interfibrillar crosslinks (pyridinoline and pyrrole) linking neighboring fibrils, and ii) non-enzymatic advanced glycation end-products (AGEs), such as pentosidine, that form both intermolecular and interfibrillar links along the collagen backbone [9]. While the level of enzymatic crosslinks stabilizes around 10-15 years of age with slight changes [10, 17], AGEs can increase up to five-fold with age [17, 63, 64]. The age-related increase of AGEs has been shown to reduce bone toughness and fracture resistance [32, 51, 65, 66]. Similarly, excessive remodeling with aging increases the osteonal density in human cortical bone; this governs the degree of microcracking and in turn affects the development of crack bridges, which provide a major source of toughening at micron-scale levels and above [62].

In this chapter, the role of aging on the mechanical properties of human cortical bone at multiple structural hierarchies is examined using a set of samples from the same donors. Using *in situ* small- and wide-angle x-ray scattering/diffraction (SAXS/WAXD) to characterize sub-micron structural changes and synchrotron x-ray computed micro-tomography and *in situ* fracture-toughness measurements in the scanning electron microscope to characterize effects at micron-scales, we show how these age-related structural changes at differing size-scales degrade both the intrinsic and extrinsic toughness of bone.

3.2. Experimental methods

3.2.1. Sample preparation

The cortical bone used in this study was from the diaphyses of fresh frozen human humeri from several age groups, specifically *Young* [34 years old (N = 1), 37 years old (N = 4) and 41 years old (N = 2)] and *Aged* [85 years old (N = 3), 91 years old (N = 1) and 99 years old (N = 2)]. *Middle-aged* bone [61 years old (N = 1), 69 years old (N = 2) and 69 years old (N = 2) years] was additionally evaluated for toughness measurements.

3.2.2. Strength and toughness testing

For strength and toughness testing, samples of bone with an approximately 2-mm width and a 1.5-mm thickness were machined from each humerus with a Buehler IsoMet 1000 precision low-speed saw. The samples for fracture toughness testing contained a notch oriented such that the nominal crack-growth direction was parallel to the long axis of the bone. Notches were applied with a low-speed diamond saw and then sharpened by repeatedly sliding a razor blade over the saw-cut notch, while continually irrigating with 1 μm diamond slurry to give final micro-notches with a reproducible root radius of ~3-5 μm; as a result, sharp cracks with an initial crack length of $a \approx 1$ mm ($0.4 \leq a/W \leq 0.6$) were generated in general accordance with ASTM standards [33]. The resulting toughness specimens were ground with successively finer grit to a 1200-grit finish prior to final polishing with a 1-μm and then a 0.05-μm diamond suspension. All samples were stored in Hanks' Balanced Salt Solution (HBSS) at 25°C for at least 12 h prior to testing.

A three-point bending configuration was used for the strength and toughness tests (with the notch directly below the top pin in the toughness test) with a displacement rate of 0.55 μm/s. The strength tests were performed with a 7.5-mm span in 25°C HBSS and were analyzed according to ASTM Standard D790-10 [67]. The fracture toughness tests were evaluated using a R-curve analysis in general accordance with ASTM Standard E1820[4] [33]. To make such measurements while simultaneously imaging the

[4] While a non-linear *J*-integral analysis is often recommended, a linear-elastic fracture mechanics (LEFM) analysis was used here (similar to Nalla *et al.* [62] for the long crack data presented in Fig. 3.2). The LEFM approach is justified by the fact that the plastic zone size, calculated as $r_y \sim \frac{1}{2\pi} K \sigma_Y^{-2}$, where σ_Y is the yield stress (120 MPa), was two orders of magnitude smaller than the in-plane and out-of-plane dimensions of the sample; thus, a state of small-scale yielding and plane strain was achieved in our samples.

initiation and growth of cracks in real time, *in situ* testing of samples soaked in HBSS was performed in a Hitachi S-4300SE/N environmental scanning electron microscope (Hitachi America, Pleasanton, CA) at 25°C using a Gatan Microtest 2-kN three-point bending stage (Gatan, Abington, UK). Images of the crack path were obtained simultaneously in back-scattered electron mode at a voltage of 25 kV and a pressure of 35 Pa. These tests were used to define the early portion of the R-curves. Crack sizes were small and as such physiologically relevant with crack extensions not exceeding ~500 μm. R-curve determination was limited to small-scale bridging conditions, where the size of the zone of crack bridges behind the crack tip remained small compared to the in-plane test specimen dimensions.

3.2.3. SAXS/WAXD testing

Rectangular samples of human cortical bone were sectioned with a Buehler IsoMet 1000 precision low-speed saw to a thickness of 0.5 mm, such that the long axis of the samples was parallel to the long axis of the bone. The samples were then polished with 800-grit paper to a final dimension of roughly 15 mm x 1 mm x 200 μm. The samples were left to dry in air for roughly 24 h before 60-grit silicon carbide paper was glued to the ends of the samples with cyanoacrylate glue to form frictional surfaces to grip during testing. The glue was left to dry for 24 h. The samples were then wrapped in HBSS-soaked gauze for at least 12 h prior to testing.

The samples were loaded in tension in a custom-made rig, with the sample held between two grips, one of which was stationary and the other connected to a displacement stage and a 5-kgf load cell (Omega, LC703-10), see Fig. 3.1. The rig was positioned in beamline 7.3.3 at the Advanced Light Source (ALS) synchrotron radiation facility (Lawrence Berkeley National Laboratory, Berkeley, CA), such that SAXS and WAXD data collection could be recorded simultaneously with mechanical loading. The testing was performed at room temperature and a displacement rate of 1 μm/s, with samples hydrated throughout the experiment by means of a hydration cell comprising a strip of cellophane held to the sample through capillary action with a few drops of HBSS.

A high-speed Pilatus detector was used to collect the SAXS data, while a Quantum CCD X-ray detector (Area Detector Systems Corporation) was used to collect the WAXD data. The SAXS detector was located at the largest allowable distance from the sample (~4100 mm) to detect fine changes in the collagen peak's position, whereas the WAXD detector was placed ~250 mm from the sample. The sample was exposed to x-rays for 0.5 s every 15 s seconds, while the detectors collected data and the strain was increased at a rate of 1 μm/s. To keep the amount of radiation absorbed by the bone to a minimum so as not to influence its mechanical properties [68], the total x-ray exposure was limited to 30 kGy, which is in the range of sterilization of bone allografts.

The strain applied to the bulk sample was measured by marking the sample with two sets of horizontal lines. A CCD camera was utilized to image the sample as the

loads were applied. The macroscopic tissue strain in the sample was determined from the change in spacing during testing of the horizontal lines on the sample. Image analysis software (National Instruments Vision Assistant 8.5) was used to find the line locations in each consecutive image through a genetic algorithm and then to calculate the number of pixels between them. The tissue strain, ε_t, applied to the samples can then be simply calculated as $\varepsilon_t = \Delta l / l_o$, where $\Delta l = l_i - l_o$ is the change in length between the lines on the sample, and l_i and l_o are, respectively, their instantaneous and initial separations.

The analysis software IGOR Pro (Wavemetrics) was used in conjunction with the custom macro NIKA (Jan Ilavsky, Argonne National Laboratory) to convert the two-dimensional SAXS data to one-dimension. The sample-to-detector distance and beam center were calibrated with the two-dimensional diffraction pattern of a silver behenate standard. A mask was created that removed the beamstop, the detector module gaps, and all hot pixels from analysis. The two-dimensional data were then converted to one-dimensional data by radially integrating over a 10° sector oriented parallel to the direction of loading. The location of the first-order collagen peak was found by fitting the one-dimensional SAXS data with a Gaussian function and a fourth-order polynomial. The strain in the collagen fibrils was measured as the change in position of the first-order collagen peak's center divided by its location at zero load.

WAXD images were calibrated using an Al standard to find the sample-to-detector distance and beam center, as above. The two-dimensional images were then converted to a one-dimensional dataset by taking a 20-pixel wide sector that was aligned with the loading axis. The (0002) peak of the mineral at roughly a lattice spacing of 0.344 nm (or a reciprocal space vector of 1.8 $Å^{-1}$) was fit with a Gaussian function and a fourth-order polynomial. The strain in the mineral was defined as the change in position of the (0002) peak divided by the location at zero load.

3.2.4. X-ray computed micro-tomography

Synchrotron x-ray computed micro-tomography was also performed at the ALS (beamline 8.3.2) to visualize in three-dimensions the distribution of secondary osteons and the interaction of the crack path with the bone-matrix structure after R-curve testing. The setup is similar to standard tomography procedures [69] in that samples are rotated in precise incremental steps in a monochromatic x-ray beam and the transmitted x-rays are imaged via a scintillator and an optics set-up to give an effective voxel size in the reconstructed three-dimensional image of 1.8 μm. The samples were scanned in absorption mode and the reconstructed images were obtained using a filtered back-projection algorithm. In absorption mode, the gray scale values of the reconstructed image are representative of the absorption coefficient. To maximize the signal to noise ratio and optimize the interaction between the x-rays and the sample, an incident x-ray energy of 18 keV was selected with an exposure time of 350 milliseconds. The final spatial resolution was 1.8 μm per voxel. The data sets were reconstructed using the

software Octopus [70] and the three-dimensional visualization was performed using Avizo™ software [71]. Reconstructed two-dimensional slices were processed further to reduce speckle noise and enhance edges through an edge preserving smoothing algorithm in ImageJ [72]. Through a series of binary pixel open, close, and erode operations the desired morphology of the bone volume was binarized. Calculations of the Haversian canal diameter were performed on the entire reconstructed slice volume using a three-dimensional ellipsoid fitting algorithm. The average osteonal density was derived from the ratio of the binary black pixels over the total image stack volume.

3.2.5. The accumulation of advanced glycation end-products

A fluorometric assay was performed to evaluate the extent of AGEs in the bone samples. A section of the humeral midshafts was demineralized using EDTA and then hydrolyzed using 6 N HCl (24 h, 110°C). AGE content was determined using fluorescence readings taken using a microplate reader at the excitation wavelength of 370 nm and emission wavelength of 440 nm. These readings were standardized to a quinine-sulfate standard and then normalized to the amount of collagen present in each bone sample. The amount of collagen for each sample was determined based on the amount of hydroxyproline, the latter being determined using a chloramine-T colorimetric assay that recorded the absorbance of the hydrolysates against a commercially available hydroxyproline standard at the wavelength of 585 nm [73].

3.3. Results

3.3.1. Mechanical properties

The *in vitro* strength and toughness properties of hydrated human cortical bone samples from diaphyses of fresh frozen humeri were examined from young and aged groups: *Young* [34 - 41 years old (N = 7)] and *Aged* [85 - 99 years old (N = 6)].[5] Strength properties, determined from the three-point bending of unnotched beams, indicate a loss in yield strength and peak strength with aging (Fig. 3.2a). Corresponding fracture toughness properties, presented in the form of stress-intensity *K*-based crack-resistance curves (R-curves)[6] in Fig. 3.2b, reveal a progressive loss in both the crack-initiation and crack-growth toughness in the longitudinal orientation with aging. These latter data represent the current measurements on small cracks sized below ~500 μm, performed *in situ* in the environmental scanning electron microscope (ESEM), together with our

[5] Middle-aged bone, 61 - 69 years old (N = 5), was additionally evaluated for toughness measurements.

[6] The crack resistance-curve provides an assessment of the fracture toughness in the presence of subcritical crack growth. It involves measurements of the crack-driving force, *e.g.*, the stress intensity *K*, strain-energy release rate *G* or *J*-integral, as a function of crack extension (Δa). The value of the driving force at $\Delta a \rightarrow 0$ provides a measure of the crack-initiation toughness whereas the slope (used in this study) and/or the maximum value of the R-curve can be used to characterize the crack-growth toughness. Indeed, the slope of a rising R-curve is directly related to the potency of the extrinsic toughening mechanism involved.

previous *ex situ* measurements [62] on the same bone, in which crack sizes were an order of magnitude larger. For this age range (34 - 99 years), the *ex situ* results indicate an age-related decrease in crack-initiation toughness by roughly a factor of two, with a much larger (six-fold) decrease in crack-growth toughness. The variation between the three group means (*Young*, *Middle Aged*, and *Aged*) was statistically significant, with p = 0.025 and 0.0036 for the crack initiation and growth toughnesses, respectively.

3.3.2. Structural characterization at micrometer scales and above

From *in situ* ESEM and *ex situ* three-dimensional synchrotron x-ray computed micro-tomography, the fracture surfaces were seen to be relatively smooth in the longitudinal orientation with crack paths showing extensive evidence of microcrack formation nominally parallel to, and ahead of, the growing crack (*i.e.*, crack bridges, see Fig. 3.3). This follows because the major microcracks form preferentially along the cement lines (*i.e.*, along the long axis of the bone). The intact regions between these microcracks and the main growing crack result in the formation of "uncracked-ligament bridges" to provide a source of extrinsic toughening by carrying load that would otherwise be used to further crack growth. As reported previously, the crack bridges were smaller and fewer in number in the *Aged* bone (see Fig. 3.3) [62], resulting in a reduced contribution to the crack-growth toughness with aging.

Three-dimensional x-ray computed micro-tomography was also used to characterize the number and size of the osteons in *Young* and *Aged* bone. Fig. 3.4 clearly demonstrates the dramatically higher number of osteons in *Aged* bone; in fact, the *Aged* sample has nearly three times the osteonal density, defined as the number of osteons per unit bone area (On.Dn.), consistent with reports in the literature [74]. The higher osteon density in *Aged* bone supports the notion that a growing crack will have more cement lines at which microcracks can form, resulting in both smaller crack bridges and a lower crack-growth toughness.

3.3.3. Structural characterization at sub-micrometer scales

To examine the corresponding intrinsic behavior at smaller (sub-micrometer) dimensions, *in situ* high-flux synchrotron x-ray scattering experiments were performed on uniaxial tensile specimens to study the mechanical behavior of the individual constituents of bone, specifically to discern the strain in the mineralized collagen fibrils and in the mineral as a function of the applied strain in the sample, *i.e.*, the tissue strain (Fig. 3.5).

Results from the SAXS/WAXD experiments are shown as strains in the mineralized collagen fibrils (Fig. 3.5a) and in the mineral[7] (Fig. 3.5b) as a function of the macroscopic strain applied to the sample (*i.e.,* the tissue strain). For a given tissue strain, the strain in the mineralized collagen fibrils is more than 25% lower in the *Aged* bone (Fig. 3.5d) than

[7] The mineral strain does not significantly change (Fig. 3.5b), principally because it has a stiffness roughly three orders of magnitude larger than the collagen.

in the *Young* bone, implying that the fibrils have become stiffer with age (*i.e.*, for a given tissue strain, the collagen fibrils in young bone have a higher strain and thus absorb more energy at this structural level through deformation).

For the stiffness of the fibrils to change with age, structural changes must be occurring at this level. To examine changes to the collagen environment with age, collagen crosslinking due to non-enzymatic glycation, *i.e.*, AGEs (Fig. 3.6) was quantified. AGEs form intra- and interfibrillarly due to a glycation reaction between the collagen molecules and sugars. Consistent with the literature [17, 63], our results show a higher level of AGEs in *Aged* bone than in *Young* bone (Fig 3.6). The SAXS/WAXD observations clearly indicate that these increased levels of non-enzymatic crosslinks with aging stiffen the collagen fibrils, thereby affecting the plasticity of the bone.

3.4. Discussion

This study shows that the mechanisms of fracture resistance in human cortical bone are derived over a range of length-scales from molecular levels to near millimeter dimensions, and that the salient strengthening and toughening mechanisms are individually related to nano/microstructural features in the bone-matrix structure. These features degrade with biological aging and lead to a deterioration in the bone strength and toughness. The macroscopic mechanical property measurements demonstrate that over the age range of ~34 to 99 years, there is a definite loss in bone quality affecting the fracture risk; specifically, there is a reduction in bone strength, initially as a loss in plasticity and subsequently in peak strength (by roughly 10% compared to *Young* bone), and a corresponding two- to six-fold decrease in fracture toughness, respectively, for crack initiation and crack growth (Fig. 3.2). However, the origin of these properties and their biological degradation reside at very different length-scales.

3.4.1. Phenomena at sub-micrometer length-scales

Mineralized collagen fibrils are the basic building blocks of the bone matrix; they consist of a self-assembly of collagen molecules and HA platelets. At this length-scale, bone deforms by stretching and unwinding of individual collagen molecules due first to entropic and then energetic mechanisms that break the H-bond [40, 75] as well as deformation of the mineral's crystalline lattice, which is primarily deposited in the gaps between the collagen molecules.

At the next length-scale, the mechanical properties of the mineralized collagen fibril reflect the composite deformation of the collagen and HA. Within the fibrils, sliding at the mineral/collagen interface [47], intermolecular crosslinking [9], and sacrificial bonding [52] constrain molecular stretching and provide the basis for the increased apparent strength of the collagen molecules without catastrophic failure of either component. These mechanisms of load transfer between the collagen molecules and HA platelets within a fibril enable a large regime of dissipative deformation once plastic

yielding begins [46]. This molecular behavior of the protein and mineral phases (fibrillar sliding) during large-scale deformation of the mineralized collagen fibrils represents the principal mechanism of plasticity at this length-scale. As in most materials, plasticity provides a major contribution to the intrinsic toughness by dissipating energy and through the formation of "plastic zones" surrounding incipient cracks that further serve to blunt crack tips, thereby reducing the driving force (*i.e.*, stress intensity) for crack propagation.

However, the strength and plasticity of bone are clearly degraded with aging. An explanation for this at the collagen fibril length-scale is offered by current *in situ* SAXS/WAXD studies, which indicate that for a given strain applied to the bone tissue, the strain carried by the collagen fibrils is significantly less, by some 25%, in *Aged* bone compared to *Young* (Fig. 3.5a). The origin of this stiffening of the collagen with aging though, can be associated with an even lower level of the hierarchy.

The measurements in this study (Fig. 3.6), and elsewhere [17, 63], demonstrate that aging results in increased inter- and intra-fibrillar AGEs crosslinks. These act to degrade the structural integrity of the fibrils by stiffening them to restrict the fibrillar sliding (plasticity) mechanism and consequently to degrade the ductility, strength, and intrinsic toughness of the bone. These results are consistent with both a theoretical fibril model [50], which has predicted an inhibition of fibrillar sliding with non-enzymatic crosslinking, and experiments [51] on cortical bone that showed a reduced toughness in glycated cortical bone from the loss of energy dissipation in the stiffened organic matrix.

Raman spectra previously acquired on the bone examined in this work also indicated increased crosslinking of the collagen molecules with aging in that the intensity of the Amide-I peak sharply increased with age [62]. Similar effects have been seen for human cortical bone subjected to increasing levels of x-radiation [68] and for the aging and demineralization/dehydration of human tooth dentin [76]. The strong intensity of the amide features observed in these mineralized tissues can be attributed to broadening of the resonance profile for the amide $\pi \rightarrow \pi^*$ transition caused by changes in the fibrillar environment of the collagen [77].

Taken as a whole, the evidence at sub-micrometer length-scales strongly suggests that aging results in changes to the collagen environment, primarily through the formation of crosslinks, which specifically act to constrain the fibril's capacity to deform. This loss of bone plasticity component at these nanometer length-scales directly degrades the intrinsic bone toughness, thereby contributing to the increased fracture risk.

3.4.2. Phenomena at micro to near-millimeter length-scales

An even greater contribution to the fracture resistance of bone, however, is at much coarser length-scales in the range of 10s to 100s of micrometers and involves mechanisms of extrinsic toughening that inhibit the growth of cracks. The primary

driver for these mechanisms is the nature of the crack path and how it interacts with the bone-matrix structure. Two salient toughening mechanisms can be identified (7,8), crack bridging and crack defection/twist; the latter occurs when the crack trajectory deviates from the path of maximum driving force, *e.g.*, the path of maximum tensile stress. Several structural features, such as osteocyte lacunae, porosity, etc., can lead to deflection of the crack path, but it is the largest features, specifically the secondary osteons, that are the most effective at deflecting cracks. The key feature here is the osteonal boundaries, the cement lines, which as hyper-mineralized regions act as primary locations for microcracking. As the osteons are aligned nominally along the long axis of the bone, the microcracks are largely oriented in this direction [61]. The crack deflection mechanism is the primary source of toughening for cracking in the transverse (breaking) orientation where these microcracks are aligned nominally perpendicular to the path of the main crack. For the longitudinal orientation under study here though, microcracks form parallel or ahead of the main growing crack, and as shown in Fig. 3.3, result in the formation of uncracked-ligament bridges. Detailed two-dimensional ESEM and three-dimensional x-ray computed micro-tomography studies show that in general the size and frequency of these crack bridges is much lower in older bone (see Fig. 3.3). We believe that this is the result of increased osteonal density and decreased size (see Fig. 3.4), which is characteristic of older bone due to a higher rate of turnover. As the nominal size of the uncracked ligaments scales with the three-dimensional osteonal spacing, the increased osteonal density leads to smaller and less frequent crack bridges associated with the extension of cracks in older bone. The marked reduction in the slope of the fracture toughness R-curves with aging (Fig. 3.2b) is completely consistent with this diminished contribution from extrinsic toughening by crack bridging.

3.4.3. Coupling of phenomena across length-scales

Fibrillar sliding plasticity mechanisms act to intrinsically toughen cortical bone at nanoscale levels, while crack deflection and bridging principally extrinsically toughen cortical bone at length-scales three orders of magnitude or so larger. Direct evidence from SAXS/WAXD experiments suggests that aging leads to a suppression of fibrillar sliding associated with increased collagen crosslinking at molecular levels. It is intriguing to contemplate whether these multi-scale mechanisms are coupled. One route is through the mechanism of microcracking, which serves as a plasticity mechanism, a source of toughening as it induces both crack deflection and bridging, and may well initiate the signaling processes that promote bone remodeling [3]. In this regard, it is pertinent to note here that the SAXS/WAXD data in Fig. 3.5a show that the strain in the mineralized collagen fibrils in *Young* bone is not that much less than the applied tissue strain (dotted line); this implies that the applied loads are being transferred far more effectively to the nanostructural length-scales in *Young* bone than *Aged*, consistent with plasticity occurring by fibrillar sliding. In *Aged* bone, conversely,

this mechanism is clearly less effective as the fibrillar strains are significantly lower than the tissue strain. Consequently, in *Aged* bone, the tissue deformation must be accommodated by mechanisms occurring at higher structural levels to compensate for lack of plasticity in the mineralized collagen fibrils. Similar conclusions have been drawn by ribosylating bone samples to induce non-enzymatic glycation *in vitro*. In particular, *in vitro* non-enzymatic glycation has been found to decrease the ability of cortical and cancellous bone to dissipate energy post yield [51, 72, 78].

A higher incidence of microcracking in aged bone [79, 80], arising from non-enzymatic crosslinking at the molecular and fibrillar level [78], is consistent with the formation of smaller crack bridges and diminished extrinsic toughening in aged bone, as shown in ref. [62]. Additionally, at the sub-micrometer length-scale, it is consistent with observations showing a higher incidence of pre- and post-yield microcracks in bone samples with higher levels of ribosylation-induced AGEs [78].

3.5. Conclusion

Human cortical bone derives its strength and toughness from mechanisms that dissipate energy at many different structural length-scales; by the same token, biological factors such as aging that impair bone quality also operate at these differing scales. In this study, we have partitioned these mechanisms into intrinsic toughening (plasticity) mechanisms such as fibrillar sliding that operate at dimensions typically below a micrometer, and extrinsic toughening (crack-tip shielding) mechanisms such as crack bridging that operate at dimensions often well above a micrometer. At the macroscopic level, aging compromises the strength, ductility (plasticity), and intrinsic toughness. Through a series of experimental multi-scale structural and mechanical characterizations, we attribute this to a series of coupled mechanisms starting at the lowest (molecular) hierarchical levels, by changing the deformation behavior of the mineralized collagen fibrils due to increased inter- and intra-fibrillar crosslinking. The resulting elevated stiffness of the collagen negatively affects the bone's ability to plastically deform, by fibrillar sliding, which then must be accommodated at higher structural levels, by increased microcracking. Coupled with an increased osteonal density in older bone, this in turn compromises the formation of crack bridges, which provide one of the main sources of extrinsic toughening in bone at length-scales in the 10s to 100s μm.

3.6. Figures

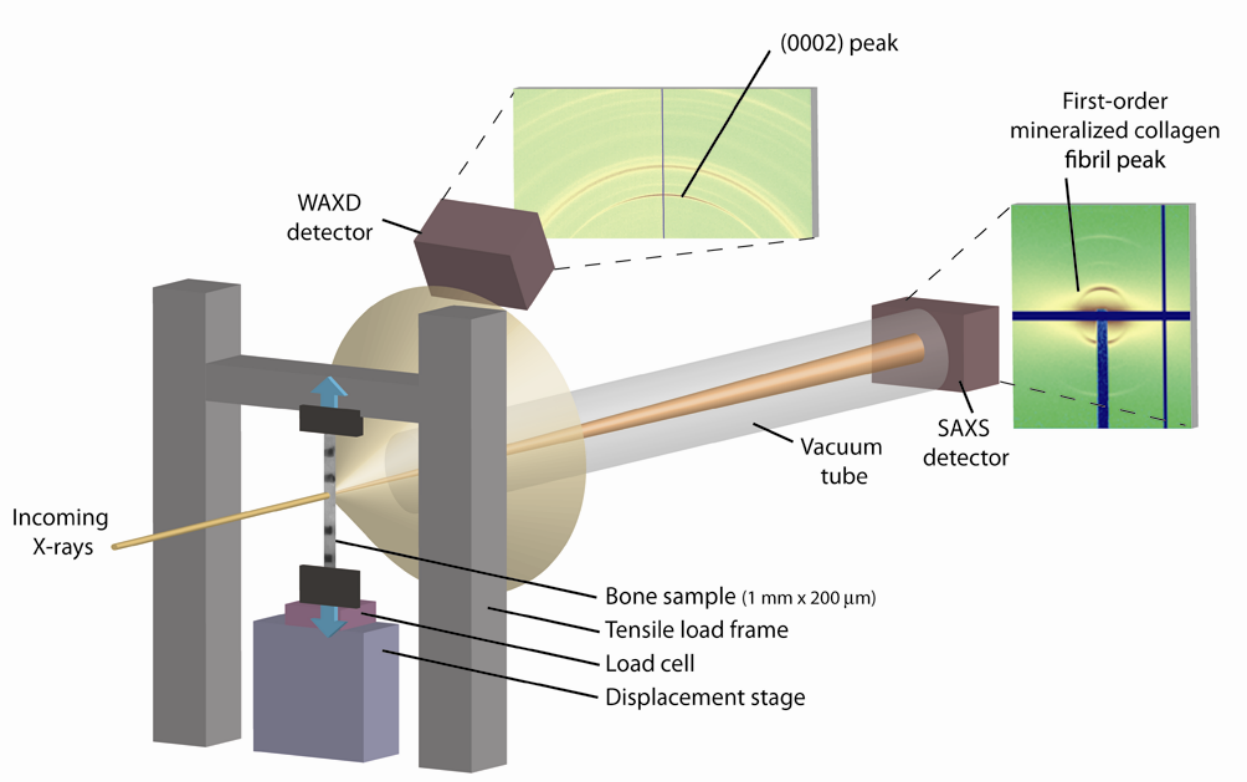

Fig. 3.1 The tension tests on both *Young* and *Aged* bone were performed with a custom built tension rig that applied displacement to the sample. Using a procedure similar to Gupta et al. [46], the samples were exposed to high-flux x-ray radiation causing the 67-nm stagger in the mineralized collagen fibril to diffract x-rays at a small angle (*i.e.*, SAXS) and the lattice of the hydroxyapatite crystals to diffract x-rays at a high angle (*i.e.*, WAXD). As load was applied to the bone, changes in the peak positions were used to calculate the mineral and fibril strains, while the tissue strain was measured with a CCD camera (not pictured).

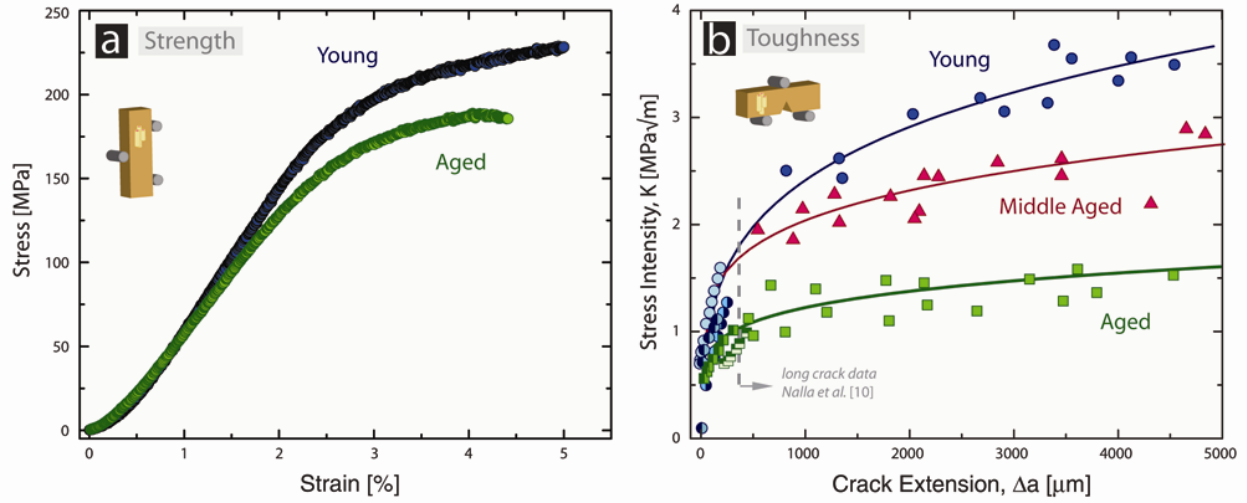

Fig. 3.2 *In vitro* mechanical properties of human cortical bone in 25°C HBSS as a function of aging showing (a) strength and (b) fracture toughness R-curve properties for the *Young* (34 – 41 years old), *Middle-Aged* (61 – 69 years old), and *Aged* (85 – 99 years old) groups. The R-curve results encompass (long crack growth) data, measured using crack sizes from ~500 μm to several mm from ref. [36], in addition to the current results on realistically short crack (< 500 μm) extensions performed *in situ* in the ESEM. The inset schematics describe the orientation of the osteons with respect to the sample geometry.

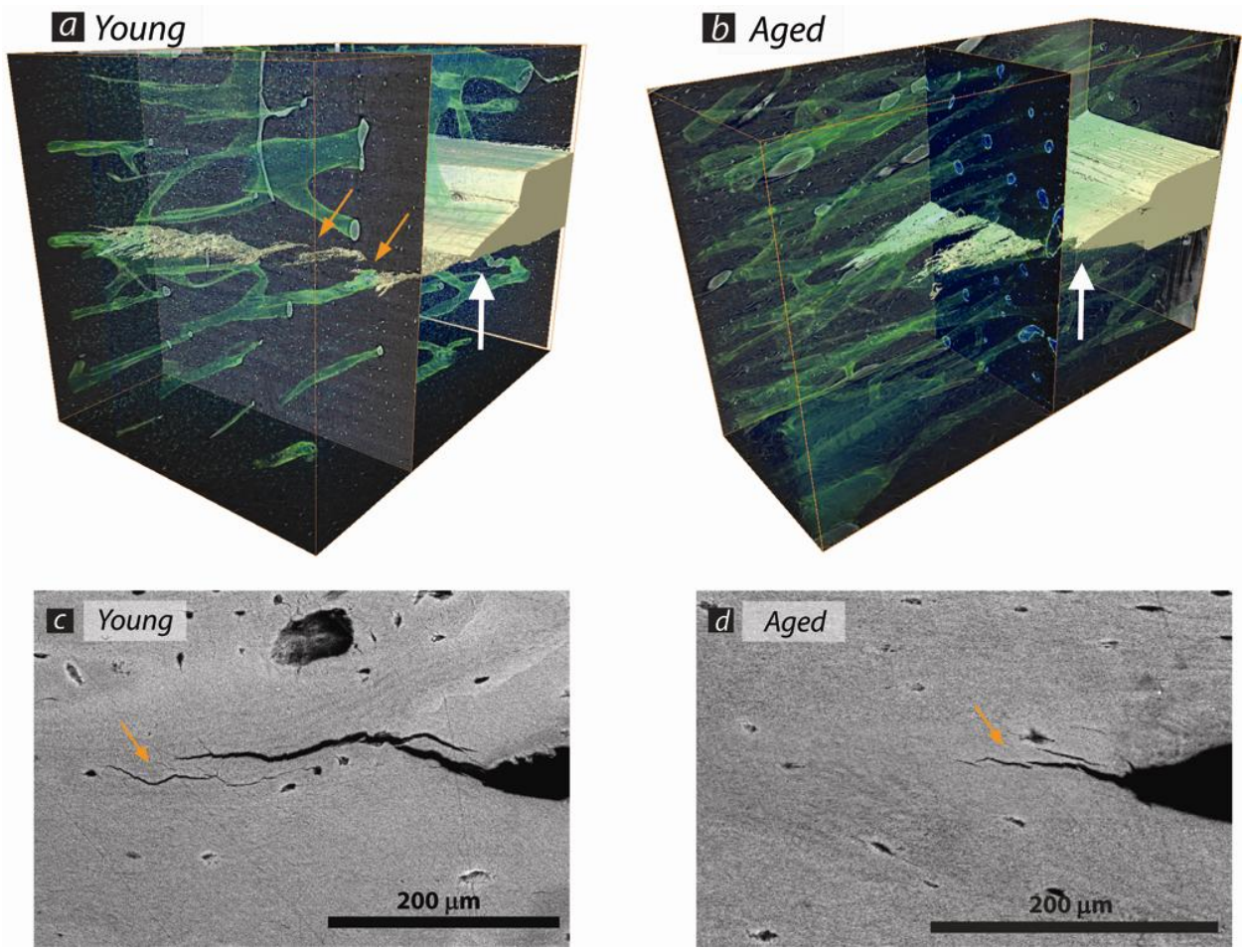

Fig. 3.3 (a, b) X-ray computed micro-tomography of *Young* and *Aged* bone samples show three-dimensional images of the crack profile after roughly 500 µm of crack growth from a razor-sharpened notch (white arrows). (c, d) SEM images during small-crack R-curve experiments confirm the presence and absence of crack bridging (other arrows) in the *Young* and *Aged* bone, respectively.

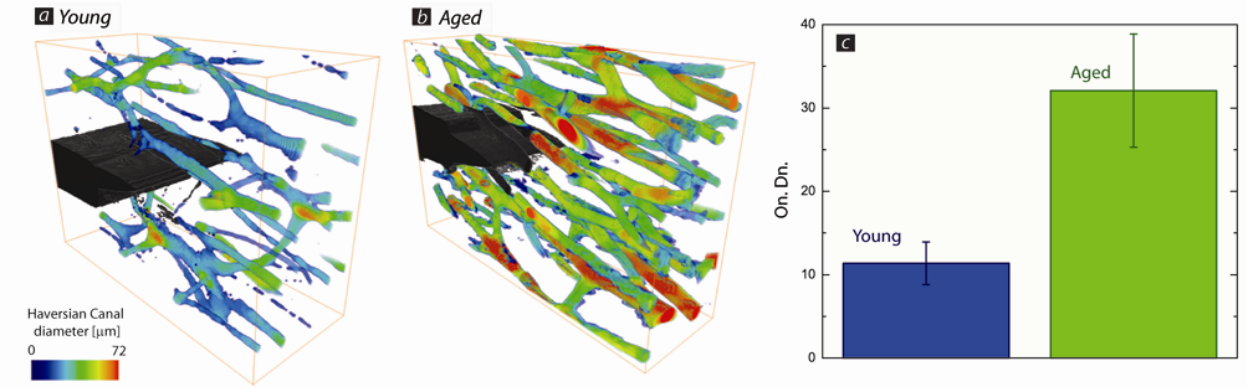

Fig. 3.4 X-ray computed micro-tomography was also used to image the size and density of Haversian canals in the (a) *Young* and (b) *Aged* human cortical bone. The color coding in (a,b) indicates the diameter of the Haversian canals. (c) As is strikingly apparent from the three-dimensional images, in terms of osteonal density (On.Dn.), the *Aged* bone has nearly three times the osteonal density than the *Young* bone. A higher volume of osteons implies more cement lines for microcracks to initiate and smaller crack bridges during crack growth.

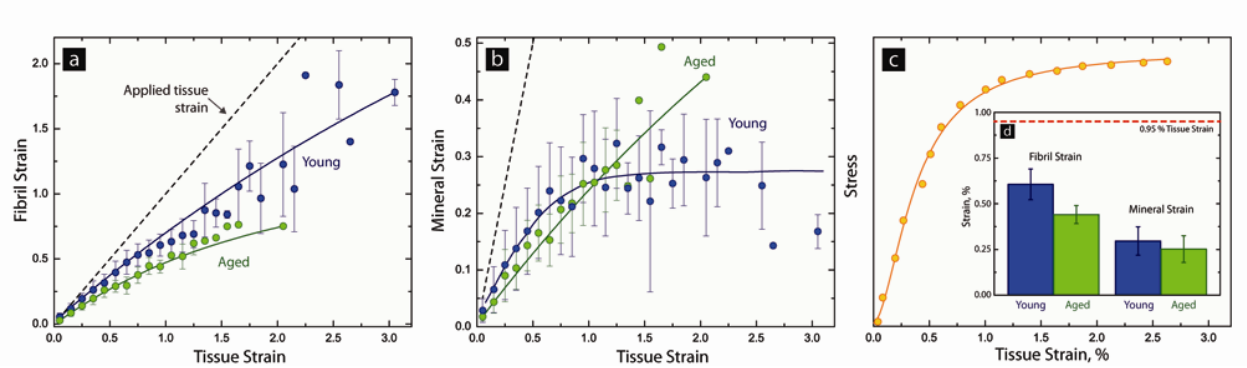

Fig. 3.5 The results of the (a) small- and (b) wide-angle x-ray scattering/diffraction experiments for tensile testing of *Young* and *Aged* cortical bone samples in the longitudinal orientation. For each individual tensile test, the strain values were binned every 0.1% tissue strain for the SAXS and WAXD experiments, respectively. For each age group, the average and standard deviation of the binned values from the tensile tests were calculated and are shown as the dots and error bars, respectively. Inset (c) shows a representative stress-strain curve for the tensile tests. (d) At a fixed tissue strain, the individual strain in the fibrils is ~25% smaller in the *Aged* bone than *Young* bone, while changes in the mineral strain are not significant.

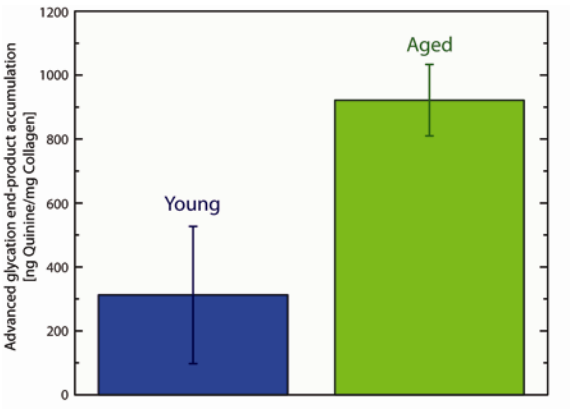

Fig. 3.6 The accumulation of advanced glycation end-products (AGEs) was fluorimetrically quantified in the cortex of the humeri in the *Young* and *Aged* bone samples. AGEs increase significantly with biological aging, with the *Aged* bone containing nearly three times as many fluorescent crosslinks as the *Young* bone. AGEs result from the reactive non-enzymatic glycation between amino residues and sugars that increases crosslinking in collagen.

Chapter 4: Mixed-mode fracture of human cortical bone

4.

4.1. Introduction

Most fracture mechanics based studies concerning the fracture resistance, or toughness, of materials have been performed under nominally uniaxial, principally tensile, loading conditions. This is mainly because, in the presence of a crack, the fracture toughness under such mode I (tensile opening) loading is invariably the worst-case, *i.e.*, the toughness in mode I is lower than under mixed-mode or mode II loading[1]. Fracture mechanics studies on human cortical bone are no exception here with the vast majority of research being focused on the mode I fracture toughness[2]. Although such research has generally been illuminating with respect to the nano/microstructural origins of fracture resistance in bone [31, 34, 37, 59], specifically for discerning the salient toughening mechanisms involved, physiologically bone is rarely loaded solely in this manner. Most cracks that are formed in bone are loaded under mixed-mode conditions created either by the shape of the bone, the nature of the *in vivo* loads, and/or the orientation of cracks with respect to these loads. Due to the anisotropy of human cortical bone and the presence of such multiaxial loading, it cannot be presumed that a crack will propagate in mode I nor whether the measured toughness values and microstructural toughening mechanisms, which have been identified in laboratory samples invariably loaded in mode I, have any relevance to *in vivo* conditions. Moreover, it has not been established for all orientations that the mode I fracture toughness is really the worst-case in a material such as bone.

In fracture mechanics terms, when a crack is loaded under mixed-mode conditions (Fig. 4.1), the crack-driving force can be described in terms of the critical strain-energy release rate, G, which can be defined in terms of the applied stress intensities, K_I, K_{II}, and K_{III}, by the following expression [81]:

$$G = \frac{K_I^2}{E'} + \frac{K_{II}^2}{E'} + \frac{K_{III}^2}{2\mu} \quad (4.1)$$

where μ is the shear modulus and E' is the Young's modulus, E, in plane stress and $E/(1-\nu^2)$ in plane strain (where ν is Poisson's ratio). For combined mode I and II

[1] In certain situations, there can be an additional out-of-plane shear loading component in mode III (anti-plane shear).

[2] The fracture toughness, K_{ic}, (where i = I, II or III) is the critical value of the stress intensity K for unstable fracture in the presence of a pre-existing crack, *i.e.*, in mode I when $K = Y\sigma_{app}(\pi a)^{1/2} = K_{Ic}$, where σ_{app} is the applied stress, a is the crack length, and Y is a function (of order unity) of crack size and geometry. Alternatively, the toughness can be expressed as a critical value of the strain-energy release rate, G_c, defined as the change in potential energy per unit increase in crack area.

loading, the mode-mixity of the applied driving force, *i.e.*, the relative proportion of K_{II} to K_I can be described by the so-called phase angle, Ψ, which is defined as:

$$\Psi = tan^{-1} \frac{K_{II}}{K_I} \quad (4.2)$$

such that the phase angles for pure mode I and pure mode II loading are, respectively, 0° and 90°.

In the presence of a crack, the application of mixed-mode loading creates both tensile (mode I) and shear (mode II) driving forces at the crack tip that invariably results in directional changes in the crack path. For this reason, the crack path trajectory has been used as a primary indicator of the underlying material behavior and has traditionally been used, along with the applied stress intensities, to formulate mixed-mode fracture criteria [82-84]. The application of pure mode I loading generates a maximum tensile driving force ahead of the crack tip, which results in coplanar crack growth; similarly, the application of pure mode II loading generates a maximum shear driving force ahead of the crack tip. However, under pure mode II conditions most materials do not exhibit coplanar crack growth [85]; instead, the crack invariably kinks at some angle, θ (Fig. 4.1c). Similarly, a mixed-mode driving force (modes I and II) also leads to crack kinking (and to crack twisting if a mode III anti-plane shear component is involved). Various fracture criteria have been developed to predict fracture and the angle of crack growth; the vast majority are based solely on the mechanical notion (and direction) of a maximum mixed-mode driving force, and pertain principally to ideally brittle materials. Two such criteria considered here are the maximum strain energy release rate criterion, G_{max}, and the $K_{II} = 0$ criterion. The G_{max} criterion assumes that the crack trajectory will follow the path along which the strain energy release rate is maximum, while the $K_{II} = 0$ criterion assumes that the crack will grow along the direction where the mode I stress intensity is at a maximum. In the literature, these two principal criteria have been used to numerically compute the direction of crack growth as a function of the phase angle in a homogeneous material [86]. Both the $K_{II} = 0$ criterion and the G_{max} criterion predict virtually identical crack paths and only differ slightly at very large phase angles. However, it must be noted that they both rely solely on a mechanical description of the crack-driving force – they make no considerations of the presence of microstructural anisotropy in the material under test, *e.g.*, to the presence of "weak" microstructural paths; moreover, by focusing on tensile-stress dominated criterion, they are largely applicable to nominally brittle materials.

Like bone, many structural components experience mixed-mode loading while in use, where it is presumed that the toughness, G_c, is lowest in mode I and increases monotonically with an increasing mode II component, as shown for a variety of materials in Fig. 4.2. As noted above, models for this behavior center on the notion of a maximum driving force, *e.g.*, G_{max}. It has been suggested that the strain energy accumulates, at higher phase angles, in part due to crack-surface interferences, *e.g.*,

those associated with frictional sliding, abrasion, and even locking of asperities between the mating crack surfaces [87-89]. However, such mechanical driving force considerations strictly pertain to homogeneous, brittle materials where the crack follows a G_{max} or $K_{II} = 0$ path. In anisotropic materials, the crack trajectory, and hence the fracture toughness, result from the competition between the path of maximum mechanical driving force and the path of "weakest resistance" in the microstructure.

Where these two directions are commensurate, predictions based solely on the maximum driving force criteria remain valid. Where they are incommensurate, complex crack path configurations often result, leading to significant crack deflections and twists; such deviations from the direction of maximum driving force act to "shield" the crack from the applied stresses/strains, *i.e.*, they lower the effective (local) stress intensity actually experienced at the crack tip, resulting in higher toughness [90]. As we show in this work, human cortical bone fractured in the transverse (breaking) orientation fits exactly into this latter category with the path of maximum driving force in mode I being essentially orthogonal to the preferred microstructural paths.

There have been only a few prior studies on the toughness of bone under mixed-mode loading. In one study, the mode II toughness of human cortical bone was found to be greater than the mode I toughness by a factor of ~3 in the longitudinal direction [91]; no results were obtained for other orientations[8]. Another study compared the mode I and mode II fracture toughness of bovine cortical bone in the longitudinal and transverse directions and again found the usual result that the mode I fracture toughness was the lower-bound [92]. However, in this latter study, the authors side-grooved their samples by as much as 50% of their original thickness; this has the effect of forcing the crack to take an (unnatural) coplanar path by suppressing the extrinsic mechanisms which deflect the crack, resulting in an artificial result.

In light of such limited results for the fracture toughness behavior of bone under multiaxial loading conditions, the objective of the present study is to characterize the mixed-mode crack-initiation fracture toughness of human cortical bone as a function of the phase angle (*i.e.*, in terms of the relative proportion of the K_{II} to K_I components). Experiments are focused on the transverse (breaking) and the longitudinal (splitting) orientation and are interpreted mechanistically in terms of the mutual competition between the preferred crack-path directions dictated by the mechanical driving force and the microstructural resistance.

4.2. Experimental methods

Fresh frozen human cadaveric femurs, from three males aged 48, 52, and 79 years of age with no known metabolic bone diseases, were used in this study (which was

[8] For definition of the transverse and longitudinal orientations with respect to the long axis of the bone (and hence the nominal direction of the osteons), see Fig. 2.2.

exempt from human subjects authorization because no identifying information was known about the donors). A total of 25 samples were tested using a notched asymmetric four-point bending test to determine the mixed-mode toughness: N=7 from the 48-year-old donor, N=11 from the 52-year–old donor, and N=7 from the 79-year–old donor. The cortical bone, taken from the diaphysis of each femur, was sectioned with an IsoMet 1000 precision low-speed saw (Buehler) into rectangular cross-sectioned beams with width W ~ 3.3-4.9 mm and thickness B ~ 2.0-3.0 mm. The samples were notched with a low-speed saw in the transverse (breaking) orientation; in this orientation, the notch is oriented such that the nominal crack-growth direction is from the periosteum to the endosteum and perpendicular to the long axis of the osteons (*out-of-plane* transverse), as shown in Fig. 2.2. The notches were sharpened by polishing at the root of the notch with a razor blade, which was irrigated with 1-μm diamond suspension, to give a final crack length of a ~ 1.3-2.6 mm. As a basis for comparison, four additional samples of human cortical bone from a 50-year-old male donor were tested in the longitudinal orientation. In these samples, the orientation of the notch was such that the nominal crack-growth direction was along the proximal-distal direction that is parallel to the long axis of the osteons (*in-plane* longitudinal), as shown in Fig. 2.2. All samples were ground with successively finer grit to a 1200-grit finish prior to a final polishing with a 1-μm and then a 0.05-μm diamond suspension. They were stored in Hanks' Balanced Salt Solution (HBSS) for at least 12 hours prior to testing.

To measure the fracture toughness while simultaneously imaging the initiation and growth of cracks in real time, *in situ* testing of samples soaked in HBSS was performed in a Hitachi S-4300SE/N environmental scanning electron microscope (ESEM) at 25°C using a Gatan Microtest 2-kN four-point bending stage; images of the crack path were obtained simultaneously in back-scattering electron mode at a voltage of 25 kV and a pressure of 35 Pa. Loading was applied under displacement control at a displacement rate of 6.67 μm/s, with an in-house machined rig to apply an asymmetric or symmetric four-point bending load to the sample. The value of the critical fracture toughness, G_c, was defined after 100 μm of crack extension. This arbitrary criteria guaranteed through-thickness cracking in all the tests, and no crack growth at locations other than the crack tip (*e.g.*, at the loading pins).

Whereas a pure mode I loading configuration (Ψ = 0°) was achieved using symmetrical four-point bending (pure bending), pure mode II loading (Ψ = 90°) and various degrees of mixed-mode (combined mode I and II) loading were obtained with similar notched bend specimens loaded asymmetrically. The asymmetric four-point bending configuration applies a constant shear force, Q, to the crack tip and a moment, M, whose magnitude varies linearly with displacement, c, from the center line of the rig (Fig. 4.3). Accordingly, the phase angle can be tuned by varying the position of the crack with respect to the center line of the rig, which results in a shear force and bending moment (both per unit thickness) at the crack tip:

$$Q = P\frac{y-x}{y+x} \text{ and } M = cQ \ , \tag{4.4}$$

where P is the applied load, and y and x are the larger and smaller loading spans, respectively, of the rig at which point the load is applied to the sample (Fig. 4.3b). For the asymmetric specimen geometry, He and Hutchinson [93] give the most recent linear-elastic stress-intensity factor solution for K_I and K_{II} in terms of the crack length, a, and the specimen width, W, as:

$$K_I = \frac{6M}{W^2}\sqrt{\pi a}F_I\left(\frac{a}{W}\right) \text{ and } K_{II} = \frac{Q}{W^{\frac{1}{2}}\left(1-a/W\right)^{\frac{3}{2}}}F_{II}\left(\frac{a}{W}\right), \tag{4.5}$$

where F_I and F_{II}, are the geometry functions tabulated, respectively, by Tada [94] and He and Hutchinson [93], and are expressed as:

$$F_I\left(\frac{a}{W}\right) = \sqrt{\frac{2W}{\pi a}}\tan\frac{\pi a}{2W}\frac{0.923+0.199\left(1-\sin\frac{\pi a}{2W}\right)^4}{\cos\frac{\pi a}{2W}},$$

$$F_{II}\left(\frac{a}{W}\right) = 7.264 - 9.37\left(\frac{a}{W}\right) + 2.74\left(\frac{a}{W}\right)^2 + 1.87\left(\frac{a}{W}\right)^3 - 1.04\left(\frac{a}{W}\right)^4 \tag{4.6}$$

As noted above, the mode I fracture toughness was measured on single-edge notched bend samples loaded in symmetric four-point bending. The loading configuration creates a region of constant moment between the inner two loading points. Thus, the stress-intensity factor solution can be obtained for an edge-cracked plate in pure bending [95], which is equivalent to the solution for K_I in asymmetric loading (Eq. 4.5), only with a moment of $M = P\frac{S_2 - S_1}{4}$, where S_2 and S_1 are, respectively, the major and minor loading spans.

The longitudinal samples were tested in asymmetric three- and four-point bend [93, 96], and in symmetric four-point bend. No crack growth was observed prior to sample failure at locations other than the crack tip. Consequently, these tests must be considered to be yielding a lower-bound for the value of the fracture toughness.

X-ray computed micro-tomography is a nondestructive characterization technique that was employed to visualize the three-dimensional mixed-mode crack path of transversely-loaded human cortical bone. The x-ray micro-tomography was performed at the Advanced Light Source synchrotron radiation facility at Lawrence Berkeley National Laboratory. Tomographic images were taken of two samples after roughly 500 μm of crack growth under either mode I or mode II loading conditions, as previously described.

The x-ray computed micro-tomography setup is similar to the standard setup for this technique [69] whereby samples are rotated (through a 180° angle) in a monochromatic x-ray beam of 20 KeV, which was chosen to maximize the signal to noise ratio. During each 180° rotation, two-dimensional images were taken every 0.25° for the mode I

sample and every 0.15° for the mode II sample. The transmitted x-rays are imaged via a scintillator, magnifying lens, and a digital camera yielding an effective voxel size in the reconstructed three-dimensional image of 1.8 μm. The samples were scanned in absorption mode and the reconstructed images were obtained using a filtered back projection algorithm. In absorption mode, the gray scale values of the reconstructed image are representative of the absorption coefficient. The data sets were reconstructed using the Octopus software [70], and the three-dimensional visualization was performed using Avizo (Mercury Computer Systems, Inc.).

4.3. Results

Results showing the variation in the fracture toughness of human cortical bone (defined in terms of the critical value of the strain energy release rate, G_c) as a function of the proportion of mode II to mode I loading (defined as the phase angle, $\Psi = \tan^{-1}(K_{II}/K_I)$) are shown in Fig. 4.4a for the transverse orientation. It is clear that regardless of age, the fracture toughness of cortical bone in this breaking orientation is not lowest for pure mode I tensile loading; rather it is highest in mode I and progressively decreases, by a factor of four or more, as the shear contribution increases, *i.e.*, with increasing phase angle. This is in stark contrast to the behavior of most materials, and indeed for cortical bone in the longitudinal orientation (Fig. 4.4b), where the toughness invariably increases with increasing phase angle. The critical G_c values reported in the longitudinal orientation (Fig. 4.4b) represent lower-bounds for the toughness as fracture invariably occurs at the loading pins in the direction of the weakest plane when using the asymmetric bending geometry in this orientation. However, the longitudinal data matches fairly well with previously reported trends for human cortical bone in the same orientation, which were measured using the compact-tension and compact-shear test specimens [91]. Taken together, these results clearly indicate that in the transverse direction, human cortical bone is significantly less resistant to fracture in shear, with a mode II fracture toughness some 25% smaller than in mode I.

Typical environmental scanning electron micrographs of the initial trajectory of the crack, following crack initiation from the sharpened notch, are shown in Fig. 4.5 as a function of the phase angle. The crack can be seen to initially propagate at an increasing angle of deflection, θ, to the through-thickness plane of the notch as the proportion of shear loading increases, *i.e.* with increasing Ψ. Also indicated is the direction of maximum mechanical driving force, α, defined here as the path of maximum strain energy release rate, G_{max}; the values used were computed using the He and Hutchinson solution for a crack in a homogenous material [86]. Fig. 4.6 illustrates the difference in the path of the maximum mechanical driving force and the actual path of crack growth in all of the transverse cortical bone samples. It is apparent that in general the crack does not follow this crack path with the deviation from this "expected" path highest at

low phase angles. Such crack-path deviations clearly indicate a marked influence of the microstructure, and its directionality, on the fracture process (Fig. 4.6).

The effects of mixed-mode loading on the through-thickness crack path in the transverse samples are clearly seen from scanning electron microscopy images of the fracture surfaces (Fig. 4.7) and x-ray computed micro-tomography images (Fig. 4.8). The fracture surface of a transverse sample loaded in pure mode I, $\Psi = 0°$ (Fig. 4.7a), has a torturous surface accounted for by crack deflection *on a scale of the order of hundreds of micrometers*, an effect which has been shown in previous studies to act as the dominant toughening mechanism [34]. Comparatively, in the sample loaded with a mode II driving force, $\Psi = 90°$ (Fig. 4.7b), gross crack deflection *on a scale on the order of millimeters* occurred but did not toughen the bone due to the fact that the directions of the maximum mechanical driving force and the "weakest" microstructural paths are nominally identical and both promote cracking in the same direction. Under such circumstances, resistance to fracture is low.

Three-dimensional synchrotron x-ray computed micro-tomography images of these bone samples further demonstrate the tortuous path of the deflected cracks in the transverse orientations where the preferred mechanical and microstructural crack paths are not coplanar (Fig. 4.8). Indeed, the three-dimensionality of these images clearly indicates that cracks additionally deflect out of plane, *i.e.*, they twist, which as shown in ref. [34] is an even more potent mechanism of toughening than in-plane deflection.

4.4. Discussion

In materials without microstructural anisotropy, cracks tend to follow the path of maximum mechanical driving force, with a consequent increase in toughness from the lower-bound mode I value with increasing phase angle. Assuming a path of maximum strain energy release rate (essentially a $K_{II} = 0$ path), application of a pure mode I stress intensity will result in crack growth that is coplanar to the original crack plane, a pure mode II stress intensity will result in deflection at a 74° angle to this plane, and a mixed-mode (I + II) stress intensity will result in crack deflection at an angle between these limits of 0° and 74°. However, for nominally transverse (breaking) fractures, behavior in human cortical bone is completely different, with the toughness decreasing relative to the amount of shear loading, making the mode II toughness the lower-bound.

Such seemingly surprising behavior can be explained in terms of the competition between the paths of maximum mechanical driving force and microstructural "weakness". In human cortical bone, the longitudinal direction invariably represents the preferred microstructural path; microcracking occurs quite readily along the osteon boundaries (cement lines), which are orientated along the long axis of the bone. Considering first pure mode I conditions, if the bone is loaded in the longitudinal (splitting) orientation, the direction of the maximum driving force and microstructural "weakness" coincide such that cracks propagate nominally in the expected longitudinal

direction (see the inset of Fig. 4.4b); resulting fracture surfaces tend to be rather smooth and the toughness relatively low [34]. Conversely, for mode I loading in the transverse (breaking) orientation, these directions are orthogonal (as noted above); cracks are mechanically driven to propagate transversely to break the bone but on encountering the weak cement-line interfaces are deflected longitudinally (see the inset of Fig. 4.4a). The fact that the preferred mechanical and microstructural paths are now incommensurate results in many deflections and twists in the crack trajectory, rough fracture surfaces and a much higher toughness - hence the observation that bone is easier to split than to break [34].

The same argument can be applied to explain behavior under mixed-mode conditions. As just described, when loaded in mode I in the transverse orientation, the preferred mechanical and microstructural paths are nominally orthogonal to each other, resulting in significant crack deflection and high toughness. Conversely, for pure mode II loading in the transverse orientation, the weakest microstructural direction remains longitudinal, *i.e.*, at 90° to the crack plane, and is now more favorably oriented (within 20°) to the path of maximum driving force, which is at ~74° to the original crack plane (see the inset of Fig. 4.4a); this results in a single crack deflection and a corresponding lower toughness. Accordingly, for the transverse orientation, since reducing the phase angle from $\Psi = 90°$ to 0° (from pure mode II to pure mode I) results in an increasing divergence of the preferred mechanical and microstructural crack paths, the toughness is expected to increase at the lower phase angles, *i.e.*, with a larger mode I component, due to the increased frequency and degree of crack deflection. In the mode I case, after the crack has deflected along the weak plane, the driving force reorients the crack with respect to the direction of the maximum driving force. This allows the deflection process to occur many times and toughen the material. In this way, deflections only serve to toughen the material when the difference between the directions of the maximum mechanical driving force and weakest microstructural paths is large.

These results may be considered to have significant consequences as to how we view the relevance and applicability of fracture mechanics as applied to bone fracture. Undoubtedly, bones *in vivo* invariably fail under mixed-mode loading conditions yet virtually all assessments of the fracture resistance of bone have to date been performed in mode I, which we now know from the current work is clearly not the limiting condition. It would seem that for future characterizations of the failure of bone, it is imperative to include some degree of multiaxial loading as it is clear that cortical bone is far less resistant to shear (as compared to tensile) loading due to the marked directionality of its osteonal microstructure.

4.5. Conclusion

Based on an experimental study of the fracture mechanics of human cortical bone tested in 25°C HBSS under mixed-load loading conditions, *i.e.,* in mode I (tensile) plus mode II (shear), the following conclusions can be made:

I. In the longitudinal (splitting) orientation, the fracture toughness of bone is lowest under pure mode I loading and increases with increasing phase angle (defined as the relative proportion of mode II to mode I stress intensities, $\Psi = \tan^{-1}(K_{II}/K_I)$). This is the characteristic behavior that is observed for many nominally brittle materials when loaded multiaxially in modes I and II.

II. In the transverse (breaking) orientation, the fracture toughness of bone is observed to display exactly the opposite behavior, in that the mode II fracture toughness is the lower-bound, with the toughness decreasing with increasing phase angle. Indeed, the mode II fracture toughness G_{IIc} is found to be ~25% or less than the mode I toughness G_{Ic}.

III. Such behavior is explained in terms of the competition between the direction of maximum crack-driving force, *e.g.*, the path of maximum G or the $K_{II} = 0$ path, and the path of least microstructural resistance, which in bone is associated with the boundaries of the osteons (cement lines), which are nominally aligned longitudinally along the long axis of the bone. In the transverse orientation, when the mechanical and microstructural preferred paths are commensurate, crack paths tend to be inclined but without subsequent deflections, fracture surfaces are smooth and the toughness relatively low. Where these paths are incommensurate, increasing the divergence between the two paths causes many deflections and twisting of the crack, rough fracture surfaces and higher toughness.

IV. For fracture in the longitudinal (splitting) orientation, the mechanical and microstructural preferred paths are essentially coplanar in pure mode I such that the resultant fracture path is longitudinal with few crack deflections and the toughness is relatively low. Increasing the phase angle results in a progressively larger deviation between the mechanical and microstructural preferred paths that lead to more crack deflections and consequently higher toughnesses. In this orientation of bone, the lowest toughness is found for pure mode I loading, which is typical behavior for many materials.

V. For fracture in the transverse orientation, conversely, the mechanical and microstructural preferred paths are most closely aligned in mode II (*i.e,* shear loading), such that the mode II toughness is the lowest. Now decreasing the phase angle (the relative amount of shear to tensile loading) results in a progressively larger deviation between the mechanical and microstructural preferred paths, leading to more crack deflection and higher toughness. In this breaking orientation, the lowest toughness of cortical bone is found for pure mode II loading, which is unusual behavior for most materials.

4.6. Figures

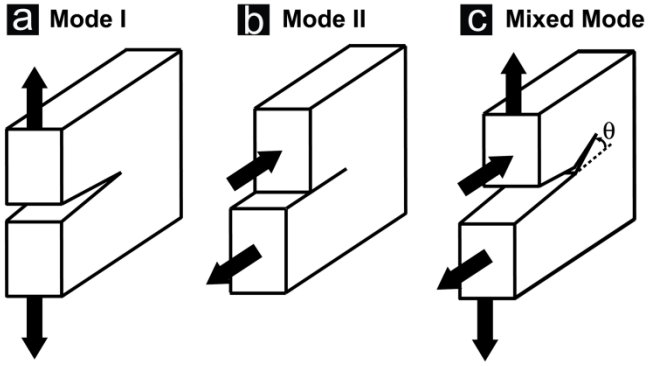

Fig. 4.1 Schematic illustrating the different modes of loading: (a) mode I (tensile loading), (b) mode II (shear loading), and (c) mixed mode. Mixed-mode loading is a superposition of the mode I and mode II stress intensities that creates a mixed-mode driving force at the crack tip; in this case, cracks are expected to grow at an angle, θ, to the original crack plane.

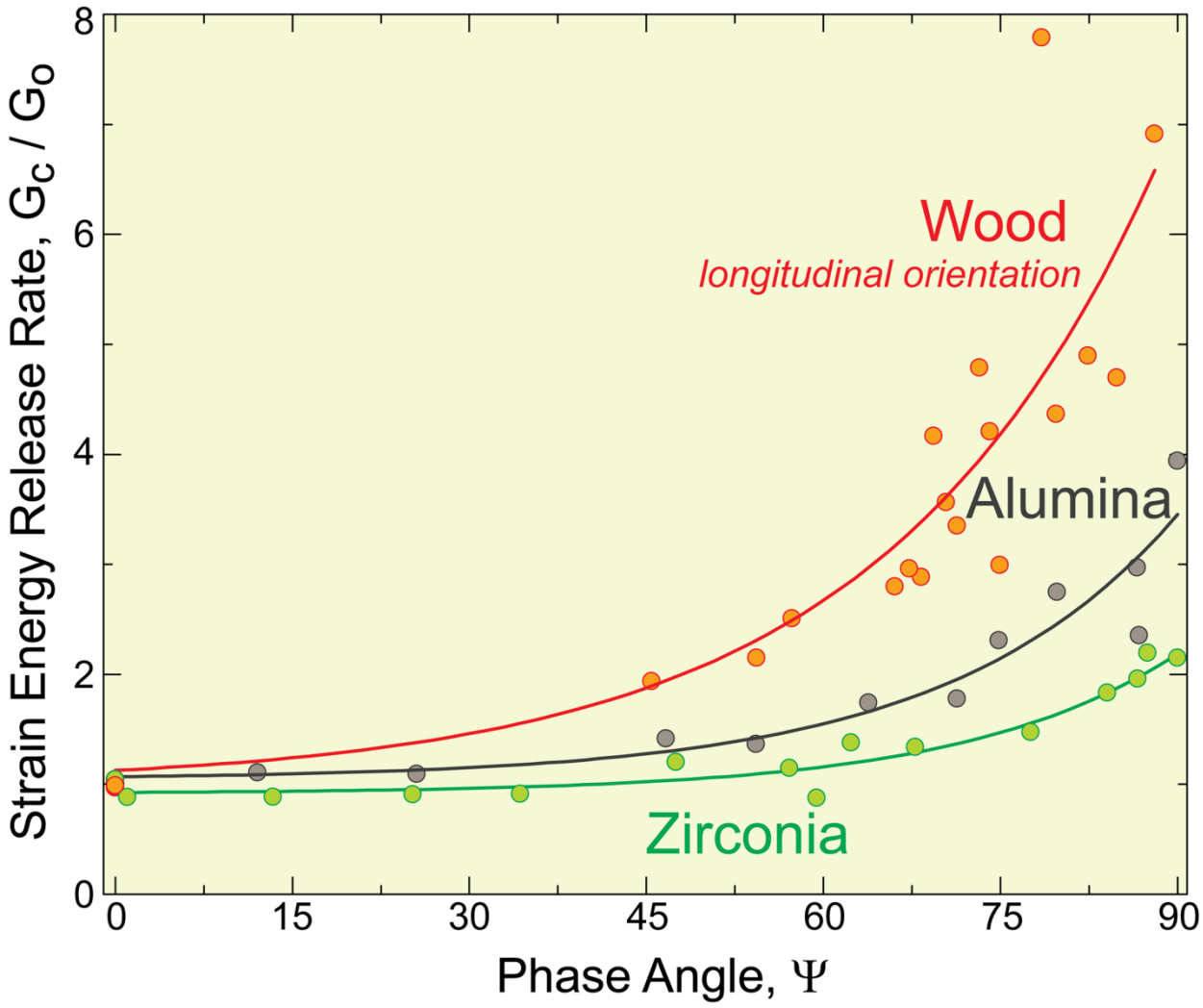

Fig. 4.2 The typical relationship between the critical strain energy release rate, G_c, and the phase angle, Ψ, for a variety of materials, namely wood (in its longitudinal direction) [97], alumina [83], and zirconia [83]. For comparison, G_c is here normalized by the lower-bound toughness, G_o. The toughness is lowest in mode I, at $\Psi = 0°$, and increases monotonically with the relative proportion of the mode II shear component until reaching a maximum under mode II conditions, at $\Psi = 90°$.

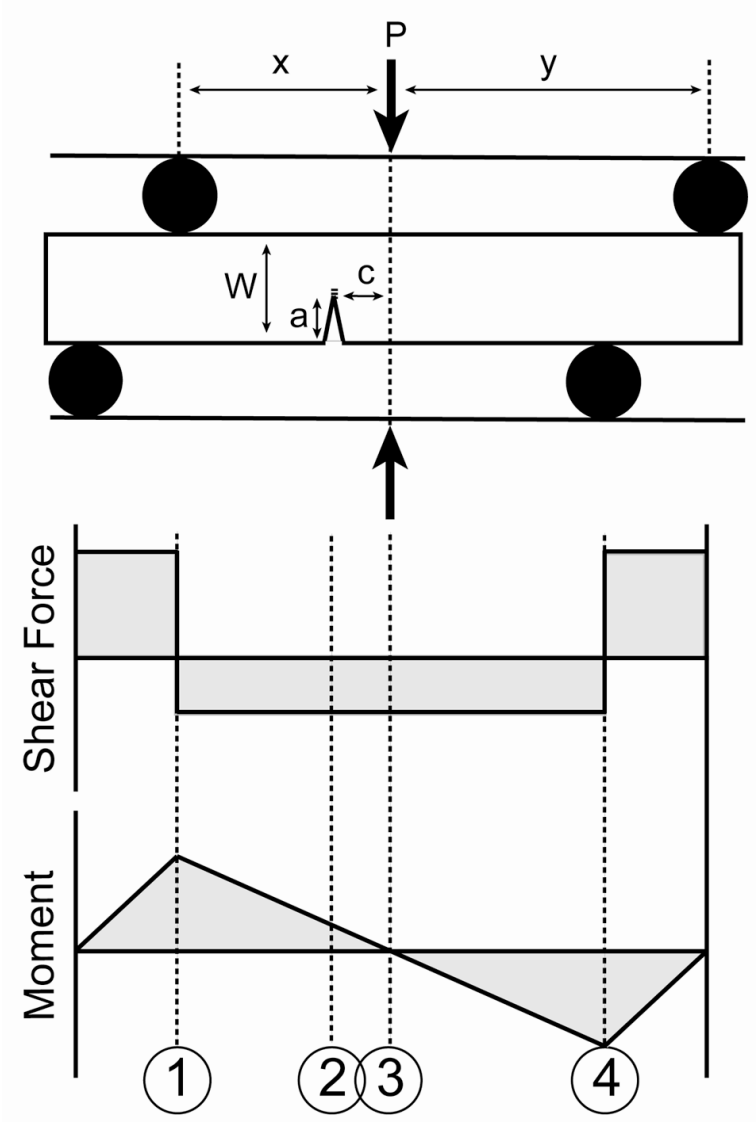

Fig. 4.3 The single-edge notched specimens were tested using an asymmetric four-point bend rig. The load is applied through the center line of the rig, which creates, through the mid-span of the sample, a constant shear force and a linearly varying bending moment. Vertical lines 1 and 4 represent the location of the inner loading pins. When the crack is aligned with the centerline of the rig, line 3, only a shear force is applied, which creates a mode II driving force. When the crack is offset from the centerline of the rig, for example line 2, a shear force and a moment are applied which creates a mixed-mode driving force. Thus, the phase angle, defined as $\Psi = \tan^{-1}(K_{II}/K_I)$, is a function of the offset of the crack, c, from the centerline.

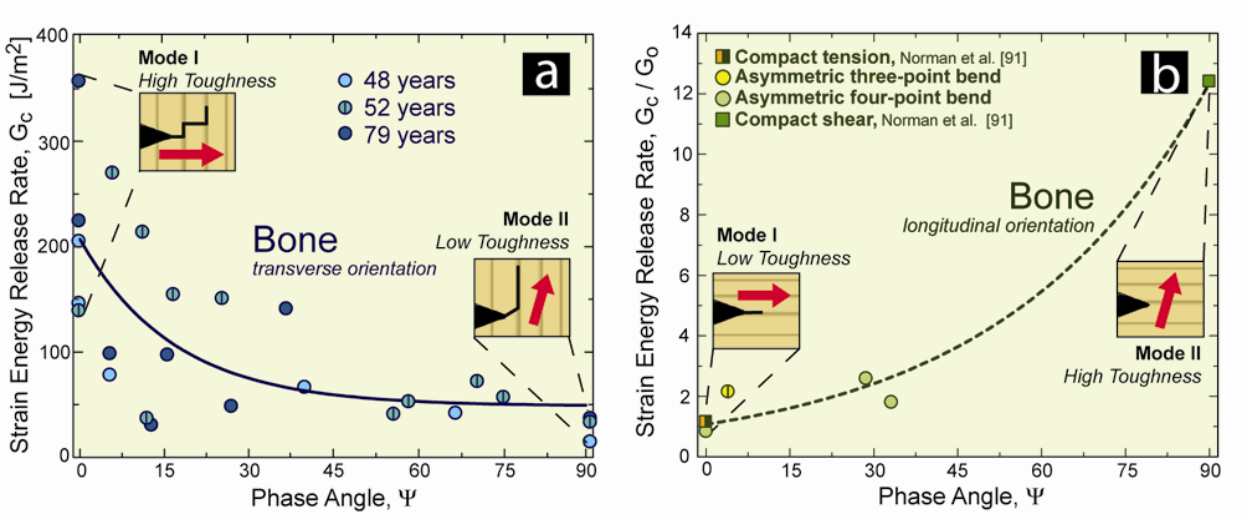

Fig. 4.4 The critical strain energy release rate, G_C, as a function of the phase angle, Ψ, is plotted for human cortical bone in the (a) transverse orientation and (b) the longitudinal orientation. The phase angle signifies the relative proportion of K_{II} to K_I; thus, for pure mode I tensile loading Ψ = 0°, while for pure mode II shear loading Ψ = 90°. While in the longitudinal orientation bone is strong in shear, the trend reverses in the transverse orientation. This unique result sheds light on the strong influence of the microstructural orientation as compared to the applied mechanical driving force. In the insets, the dark brown lines indicate the direction of the weak microstructural planes, while the pink arrows indicate the direction of the maximum mechanical applied driving force (*i.e.*, G_{max} or K_{II}=0), which in mode I is coplanar with the original crack plane and in mode II is at about a 74° angle to the original crack plane [86]. Thus, a high toughness results when the driving force is perpendicular to the weak planes (transverse mode I and longitudinal mode II). As the preferred mechanical and microstructural directions get closer to alignment, the toughness correspondingly decreases. **The longitudinal data represent a lower-bound for the expected values and are compared to data from Norman *et al*. [91].

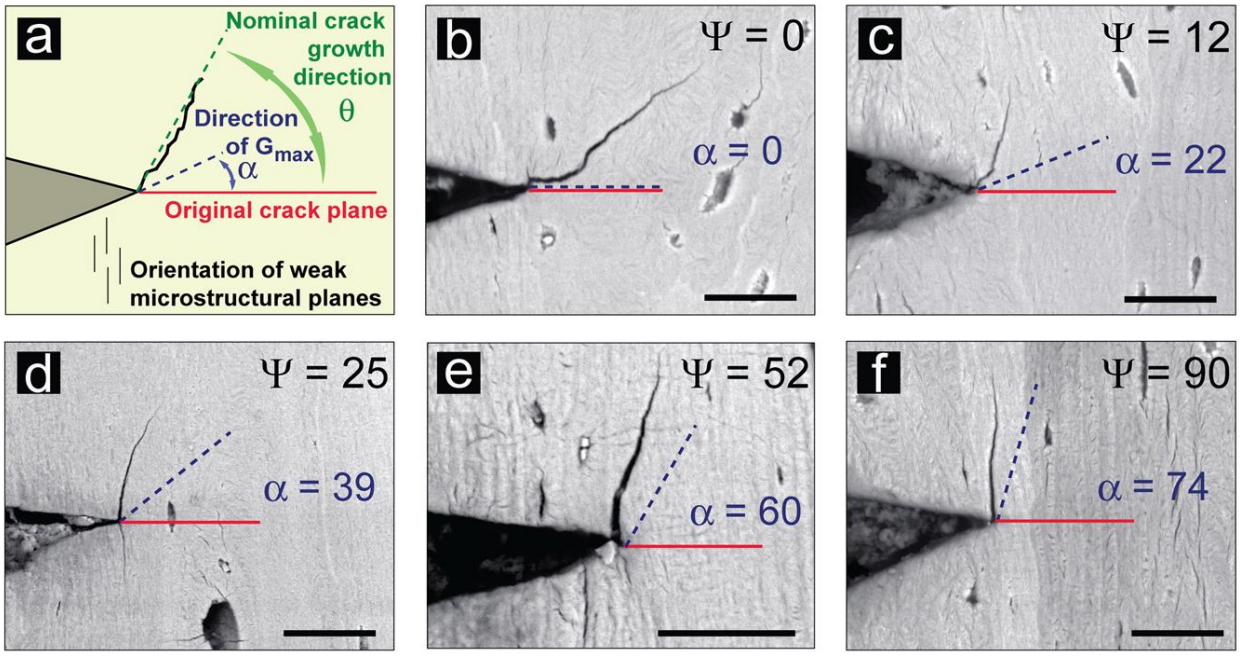

Fig. 4.5 Environmental scanning electron microscope (ESEM) backscattered-electron images of stable crack growth during *in situ* testing in the transverse orientation for phase angles of (b) $\Psi = 0°$, (c) $\Psi = 12°$, (d) $\Psi = 25°$, (e) $\Psi = 52°$, and (f) $\Psi = 90°$. (a) The crack growth angle, θ, (in green), with respect to the original crack plane (in red), increases with the phase angle. The direction of maximum driving force (in blue) is also indicated and is defined here as the G_{max} path [86]. In (b-f), the scale bars are 50 μm.

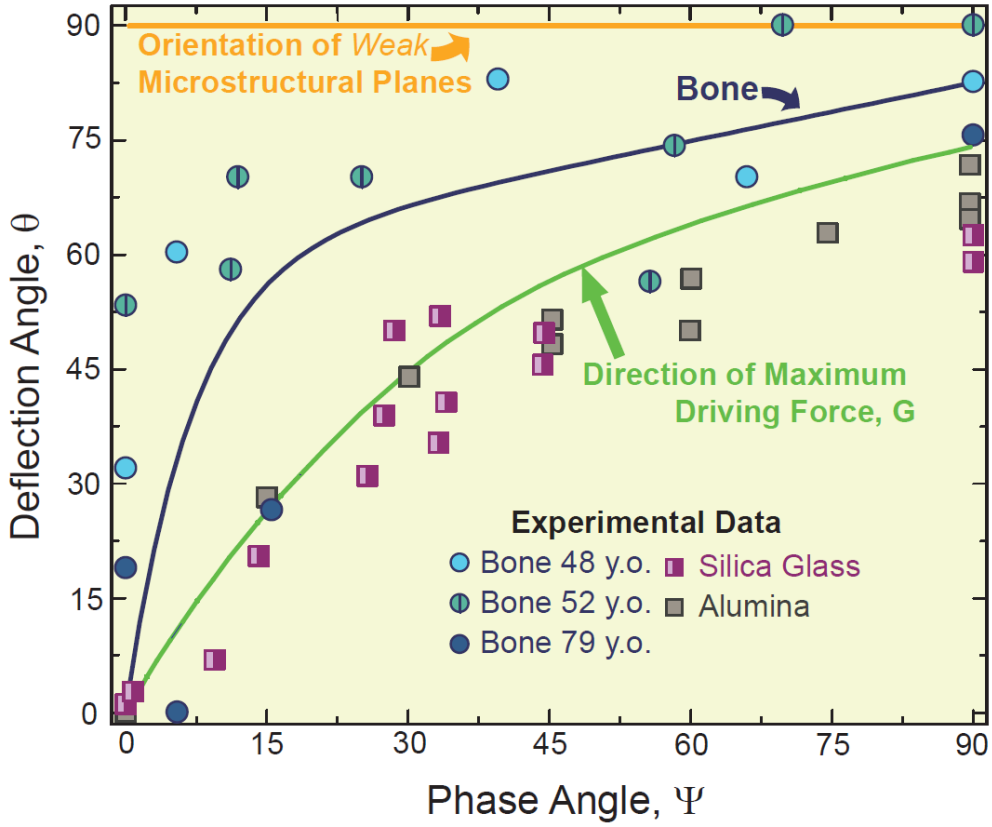

Fig. 4.6 Experimental crack deflection angle, θ, as a function of phase angle, Ψ, for human cortical bone in the transverse orientation, silica glass [98], and alumina [83]. The green line indicates the predicted angle of deflection as a function of phase angle for a material following the maximum driving force condition, G_{max}, [86] while the orange line indicates the position of the weak planes in this geometry. Traditional brittle materials follow the maximum driving force condition when a mixed-mode load is applied. However, application of a shear force in addition to the tensile force causes the direction of the driving force to change such that deflection along the weak microstructural planes becomes increasingly promoted.

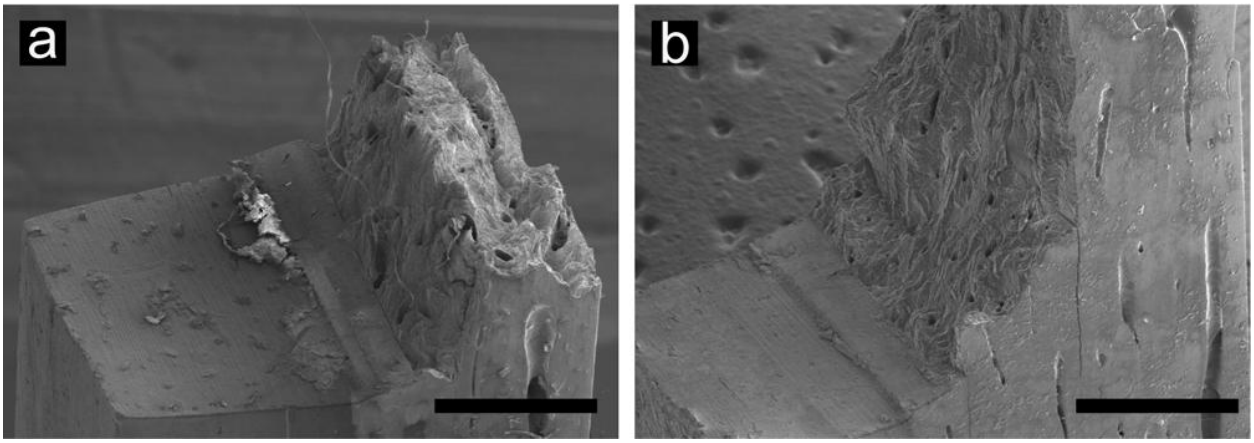

Fig. 4.7 SEM fractography images of human cortical bone after *in situ* testing in the transverse orientations for phase angles of (a) Ψ= 0° and (b) Ψ= 90°. The mode I sample shows a torturous crack path due to the disparity between the orientation of the driving force and the weak microstructural path; this toughens the material. The mode II sample shows a macroscopic inclination of the crack, on the order of millimeters, which is promoted by the alignment of the driving force and the weak planes; this contributes little to the toughness of the material. In (a) and (b), the scale bars are 1 mm.

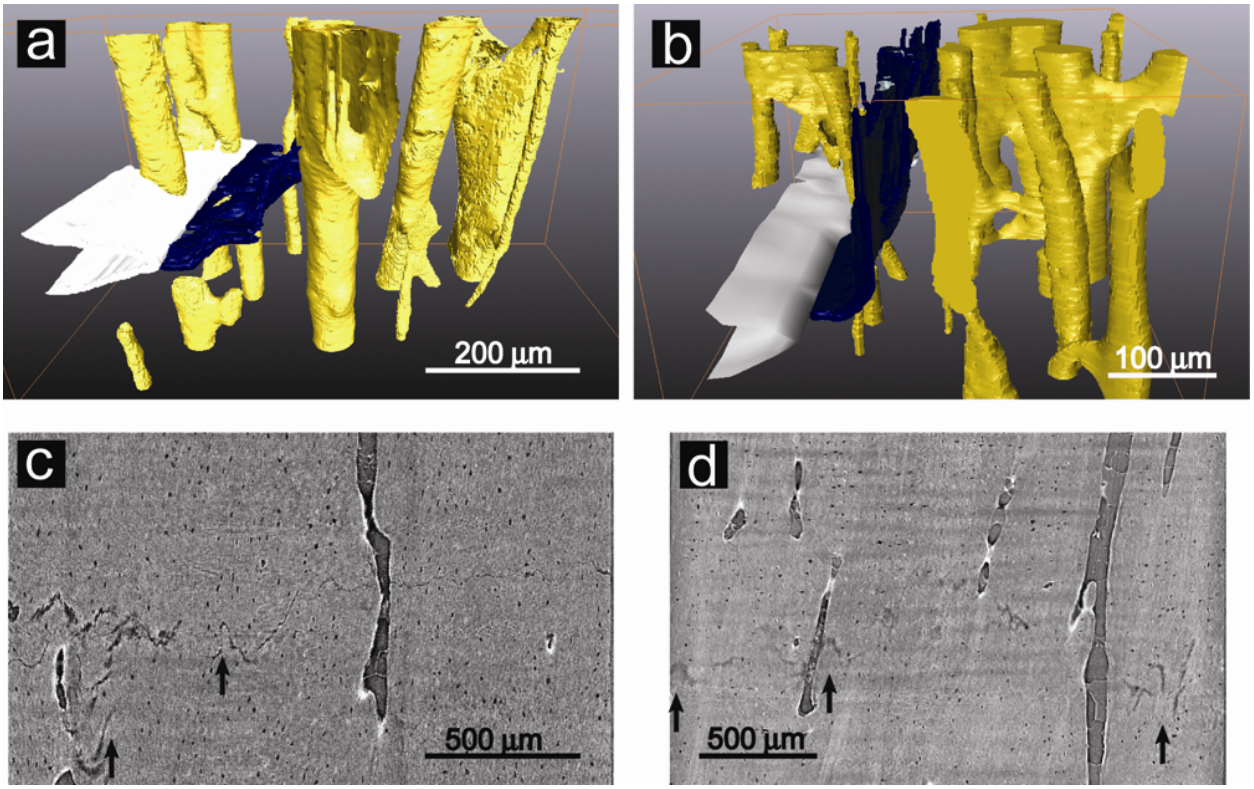

Fig. 4.8 X-ray computed micro-tomography images of human cortical bone after *in situ* testing in the transverse orientation for phase angles of (a,c) Ψ= 0° and (b,d) Ψ= 72°. In (a) and (b), the notch is colored white, the crack growth is in blue, and the Haversian canals are yellow. (a) The three-dimensional image of the mode I sample shows nominally straight crack growth with a deflection as the crack approaches a Haversian canal while the high phase angle sample (b) shows one large deflection. Images (c) and (d) are the crack paths from the back-face of the sample, *i.e.*, the crack is growing into the image. Both the high phase angle sample and the mode I sample, exhibit crack bridging and twisting. The arrows point to areas of high-angle twisting.

Chapter 5: Mixed-mode resistance-curve evaluation of human cortical bone

5.

5.1. Introduction

Bone fracture is a complex phenomenon that may be understood from the perspective of the multi-dimensional hierarchical nature of the bone-matrix structure [20, 99]. Resistance to such bone fracture, which is characterized macroscopically by such parameters as the work-of-fracture and the fracture toughness, evolves from a suite of physical structure-related mechanisms that act at multiple length-scales ranging from nano- to near macro-scale dimensions [40, 75]. These mechanisms can be classified as "plasticity" mechanisms, that operate principally at sub-micrometer dimensions to promote intrinsic toughness (*i.e.,* molecular uncoiling of collagen molecules, fibrillar sliding of both mineralized collagen fibrils and individual collagen fibers, and microcracking), and crack-tip shielding mechanisms, that operate at length-scales of ~1 to 100 μm to promote extrinsic crack-growth toughness (*i.e.,* crack deflection/twist and crack bridging). A central factor of the latter toughening mechanisms is the specific nature of the crack path that is controlled by the applied forces and the nature of the bone-matrix microstructure, in particular the hyper-mineralized interfaces of the osteons (cement lines) (Fig. 2.1), which provide microstructurally 'weak', and hence preferred, paths for cracking. As the osteons are aligned nominally along the long axis of the bone, this is the basis of the marked anisotropy in the fracture properties of bone, in that bone is easier to split than to break [28, 34, 100-102] and that the transverse toughness is lower in shear than in tension [34, 103, 104].

Fracture mechanics measurements afford the most appropriate methodology to characterize the toughness of bone by providing a quantitative measure of its fracture resistance. However, although bones invariably fracture under complex loading conditions, most measurements to date have involved solely tensile (mode I) loading with linear-elastic fracture mechanics assessments of the K_{Ic} fracture toughness, *i.e.*, the critical value of the mode I stress-intensity factor at the onset of failure. This has been reasoned to be appropriate because for most materials [83, 89], the fracture toughness under mode I (tensile loading) is generally the worst-case. However, the previous chapter showed that for human cortical bone in the transverse (breaking) orientation, the fracture toughness in shear is significantly lower than in tension, *i.e.*, the mode I toughness is *not* the worst-case (Fig. 4.4b). This is significant as physiologically bones are rarely loaded uniaxially and instead are subjected to highly mixed-mode combinations of tension, compression, and shear, depending on the character of the applied forces that they experience, the shape of the bone (*i.e.*, how the loads are transferred to a crack), and most notably, the orientation of the crack with respect to the

applied loads. Consequently, a more appropriate measure of the fracture resistance of bone must be a mixed-mode fracture toughness comprising contributions from mode I (tensile), mode II (shear), and/or mode III (anti-plane shear) crack displacements (Fig. 4.1).

Such measurements can be made for human cortical bone based on a critical value of the strain-energy release rate, G_c, where G is defined in terms of the mode I, II, and III stress intensities (respectively K_I, K_{II}, and K_{III}) as follows:

$$G = \frac{K_I^2}{E'} + \frac{K_{II}^2}{E'} + \frac{K_{III}^2}{2\mu} \qquad (5.1)$$

where μ is the shear modulus and $E' = E$ (Young's modulus) in plane stress and $E/(1 - \nu^2)$ in plane strain (ν is Poisson's ratio).

Although evaluating the toughness of bone under more complex loading is an important first step, single-value LEFM toughness parameters based on crack initiation, such as K_{Ic} and G_c, cannot truly capture, or even represent, the multiple length-scale toughening mechanisms (both extrinsic and intrinsic) acting in cortical bone, where the majority of the toughness is derived during crack growth (not crack initiation). As a result, stable (subcritical) cracking precedes outright fracture such that the fracture toughness is better characterized by rising resistance-curve (R-curve) behavior, where the fracture resistance actually increases with crack extension.

Accordingly, in this study, we attempt the first resistance-curve characterization of the fracture toughness of human cortical bone under mixed-mode loading conditions, specifically using symmetrical and asymmetrical notched four-point bend testing under combinations of mode I tension and mode II shear (Fig. 4.3), defined in terms of the phase angle, $\Psi = \tan^{-1}(K_{II}/K_I)$, where K_{II}/K_I is the mode-mixity. The resulting toughness, for phase angles between 0° and 90°, is found to depend strongly on the crack trajectory and to result from the competition between the paths of maximum mechanical driving force and "weakest" microstructural resistance.

5.2. Experimental methods

5.2.1. Mixed-mode resistance curve measurements

Fresh frozen human cadaveric femurs, from three males aged 48, 52, and 79 years of age, with no known metabolic bone diseases, were used in this study (which was exempt from human subjects authorization because no identifying information was known about the donors). A total of 12 samples were tested in the transverse orientation using notched symmetric and asymmetric four-point bending tests to determine the mode I and mixed-mode fracture toughness, respectively: N=2 from the 48-year-old donor, N=7 from the 52-year–old donor, and N=3 from the 79-year–old donor. The cortical bone, taken from the diaphysis of each femur, was sectioned with an IsoMet 1000 precision low-speed saw (Buehler) into rectangular cross-sectioned beams with a width W ~ 3.1-4.9 mm and a thickness B ~ 2.0-3.4 mm. The samples were

notched with a low-speed saw in the transverse (breaking) orientation; in this orientation, the notch is oriented such that the nominal crack-growth direction is from the periosteum to the endosteum and perpendicular to the long axis of the osteons (*out-of-plane* transverse), as shown in Fig. 2.2. The notches were sharpened by a micro-notching procedure involving polishing at the root of the notch with a razor blade, which was irrigated with 1-μm diamond suspension, to give a final crack length of a_o ~ 1.8-2.6 mm ($0.41 \leq a_0/W \leq 0.60$) with a reproducible root radius of 3-5 μm. The resulting single-edge notched bend SE(B) specimens were ground with successively finer grit to a 1200-grit finish prior to final polishing with a 1-μm and then a 0.05-μm diamond suspension. All samples were stored in Hanks' Balanced Salt Solution (HBSS) for at least 12 hrs prior to testing.

The asymmetric four-point bend geometry (Fig. 4.3) was used to measure the R-curves under mixed-mode (mode I + II) and pure mode II ($\Psi = 90°$) conditions, while a pure mode I loading configuration ($\Psi = 0°$) was achieved by using symmetrical four-point bending (pure bending) of the notched beams. To measure the crack-growth toughness while simultaneously imaging the initiation and growth of cracks in real time, *in situ* testing of samples soaked in HBSS was performed in a Hitachi S-4300SE/N environmental scanning electron microscope (ESEM) at 25°C using a Gatan Microtest 2-kN four-point bending stage; images of the crack path were obtained simultaneously in back-scattered electron mode at a voltage of 25 kV and a pressure of 35 Pa. Loading was applied under displacement control at a displacement rate of 6.67 μm/s, with an in-house machined rig to apply the asymmetric or symmetric four-point bending load to the sample.

A static equilibrium analysis of the asymmetric four-point bending configuration reveals that a constant shear force, Q, (per unit thickness) is applied to the crack tip along with a moment, M, whose magnitude varies linearly with displacement, c, from the center line of the rig (Fig. 4.3):

$$Q = P\frac{y-x}{y+x} \quad \text{and} \quad M = cQ, \tag{5.2}$$

where P is the applied load, and y and x are the larger and smaller loading spans, respectively, of the rig at which point the load is applied to the sample (Fig. 4.3). Accordingly, the phase angle, Ψ, can be tuned by varying the position of the crack with respect to the center line of the rig.

5.2.2. Stress intensity calculations

For the asymmetric four-point bend geometry, the stress-intensity factors K_I and K_{II} were determined by using the linear-elastic solution that was numerically determined by He and Hutchinson [93], such that:

$$K_I = \frac{6M}{W^2}\sqrt{\pi a}F_I\left(\frac{a}{W}\right) \quad \text{and} \quad K_{II} = \frac{Q}{W^{\frac{1}{2}}}\frac{a\ W^{\frac{3}{2}}}{1-a\ W^{\frac{1}{2}}}F_{II}\left(\frac{a}{W}\right). \tag{5.3}$$

F_I and F_{II}, are the geometry functions tabulated, respectively, in Tada [94] and He and Hutchinson [93], and expressed as follows:

$$F_I\left(\frac{a}{W}\right) = \sqrt{\frac{2W}{\pi a}\tan\frac{\pi a}{2W}}\,\frac{0.923+0.199\left(1-\sin\frac{\pi a}{2W}\right)^4}{\cos\frac{\pi a}{2W}}$$

$$F_{II}\left(\frac{a}{W}\right) = 7.264 - 9.37\left(\frac{a}{W}\right) + 2.74\left(\frac{a}{W}\right)^2 + 1.87\left(\frac{a}{W}\right)^3 - 1.04\left(\frac{a}{W}\right)^4 . \quad (5.4)$$

In symmetric four-point bending (mode I), the loading configuration creates a region of constant moment between the two inner loading points. Stress-intensity factors can be computed from the standard solution for an edge-cracked plate in pure bending [95], which is equivalent to the solution for K_I in asymmetric loading (Eq. 5.3), only with a moment of $M = P(S_2 - S_1)/4$, where S_2 and S_1 are the outer and inner loading span, respectively.

The asymmetric and symmetric four-point bend stress-intensity solutions are only applicable to coplanar crack growth. If the crack follows a deflected path, the new orientation of the crack tip with respect to the loading changes the stress field and thus, the stress intensities at the crack tip. To calculate the stress intensities at the tip of a deflected crack, the asymmetric four-point bending stress intensity solution must be modified. Many numerical solutions exist for determining the local stress intensities at the tip of a deflected crack [60, 86, 105-109] for a very small amount of crack growth. The solution of He and Hutchinson [86], for a kinked crack[9] in a homogeneous material, was chosen for this analysis due to its validity for deflection angles of more than 90° relative to the original crack plane.

To calculate the stress intensity at the tip of a deflected crack, the *global* stress intensities, K_I and K_{II} (see Fig. 5.1a), were first calculated with the asymmetric four-point bend solution for an equivalent crack of length, a:

$$a = a_o + \Delta a_p, \quad (5.5)$$

where a_o is the original crack length and Δa_p is equal to the projected length of the growing crack onto the plane of the original crack (Fig. 5.1a). The *global* stress intensities, K_I and K_{II} (Fig. 5.1a), were then converted to the *local* stress intensities, k_1 and k_2, effective at the crack tip, by using the following equations, which were numerically derived by He and Hutchinson for a kinked crack in a homogeneous material [86]:

$$k_1 = \left(c_R + d_R\right)K_I - \left(c_I + d_I\right)K_{II} ,$$
$$k_2 = \left(c_I - d_I\right)K_I + \left(c_R - d_R\right)K_{II} , \quad (5.6)$$

where c_R, d_R, c_I, and d_I are all constants that tabulated in ref. [110] as a function of the deflection angle, θ (see Fig. 5.1b), which is the angle of crack deflection with respect to the original crack plane.

5.2.3. *Resistance-curve analysis*

[9] A kinked crack is defined as a semi-finite crack with a small kink at the tip ($\Delta a/a_o \ll 1$).

For each increment of crack growth, the stress intensities at the crack tip were calculated, as previously described, in terms of the kinked crack and asymmetric or symmetric four-point bend solutions. To compute a mixed-mode driving force, the strain-energy release rate, G, was calculated from the *local* mode I and mode II stress intensity factors, k_1 and k_2, at the tip of the kinked crack:

$$G = \frac{k_1^2}{E} + \frac{k_2^2}{E} + \frac{k_3^2}{2\mu} \ , \qquad (5.7)$$

which is the same form as Eq. 5.1, with the Young's modulus E = 20 GPa for bone, and the mode III component set to zero.

The preferred *mechanically-driven* path of the crack is governed by the direction of the maximum driving force, *i.e.*, a path of maximum G; this is essentially equivalent to a zero phase-angle crack path, governed by $K_{II} = 0$. However, assessing the direction of the driving force during crack growth is a complex calculation. We have estimated the direction of the driving force by first calculating a local phase angle, determined using *local* stress intensities, *i.e.*, $\varphi = \tan^{-1}\ k_2\ \ k_1\ $, for each increment of the kinked crack; the local phase angle can then be used to determine a kink angle from the numerically based relationship computed by He and Hutchinson [86]. The direction of the driving force is the crack deflection angle minus the kink angle (see Fig. 5.1b).

5.3. Results

G-Δa R-curves for the transverse orientation loaded in pure mode I (Ψ = 0°) and at low (Ψ = 12-25°) and high (Ψ = 55-90°) phase angles are shown in Fig. 5.2. The driving force-crack extension data are replotted in Fig. 5.3 as three-dimensional R-curves, where the third axis is the phase angle, Ψ.

5.3.1. Mode I R-curves

For the transverse orientation loaded in mode I, the preferred mechanical (G_{max}) crack path and preferred microstructural crack paths (along the cement lines) are initially perpendicular. The crack begins to extend when the applied driving force exceeds the crack-initiation toughness[10]; with subsequent (subcritical) crack extension over several hundred micrometers, an increased applied driving force is required to sustain cracking (Fig. 5.2a) due to the creation of extrinsic toughening mechanisms, such as crack deflection and bridging, with crack growth. The crack-growth toughness can be defined by a linear fit to the slope of the R-curve, and ranges in this orientation from 0.43 to 2.39 J/m^2/μm in mode I. Thus, the toughness of bone increases as the crack advances with an increasing driving force required to cause further extension. Even though there are sample-to-sample variations in the magnitude and shape of the R-

[10] The initial point on the R-curve, the crack-initiation toughness, is often difficult to measure as its value depends critically on the nature and especially the sharpness of the pre-crack (or micro-notch) from which fracture ensues. However, the small number of data points collected in this study does not allow for an accurate measure of the initiation toughness to be made.

curves, the toughness of the bone exceeds G = 200 J/m^2 after at least 200 μm of crack growth.

Similarly in Fig. 5.4, sample R-curves are shown with an image of their final crack length; the amount of crack extension at each increment of crack growth is marked with a dotted blue line, while the direction of the driving force is indicated in orange. As the crack advances in mode I, the driving force remains perpendicular to the preferred microstructural direction (Fig. 5.4a), *i.e.*, the preferred direction of the mechanical (G_{max}) path remains parallel to the original crack, even though the crack deflects out of the original crack plane (shown by the deflection angle, θ, in Fig. 5.4a). When the preferred direction of the mechanical driving force is perpendicular to the preferred microstructural path, the process of such crack deflection acts as a potent toughening mechanism because it leads to a reduction in the stress intensity locally experienced at the crack tip; for a mode I crack subject to a simple in-plane deflection of 90°, the local stress is reduced by roughly 50% [60, 106]. Thus, the bone-matrix microstructure regulates the crack path by causing crack deflections principally at cement lines [34], which in turn results in an increase in the toughness with crack extension, *i.e.*, rising R-curve behavior; the toughness is further enhanced as the number of deflections or their severity increases. Thus, the highest toughness will be measured for cracks that deflect along the preferred microstructural path, while the G_{max} direction remains constant (0° from the original crack plane).

5.3.2. Mode II R-curves

In mode II, the direction of the mechanical driving force (~74° from the original crack plane) and the direction of the preferred microstructural path (~90° from the original crack plane) are nearly commensurate before crack extension begins (consistent with the low toughness of bone in shear). The crack-growth toughness for subsequent crack extension over several hundred micrometers was 0.33 J/m^2/μm (Fig. 5.2c) for both mode II R-curves. Thus, akin to mode I, the toughness increases with crack extension but to a smaller extent. Even though the toughness in mode II does increase by a factor of two over ~ 50 - 150 μm in crack growth, the maximum toughness never exceeds G = 80 J/m^2. Thus, in mode II, the onset of outright fracture or instability, *i.e.*, unstable cracking, is reached faster than mode I because the R-curves are shallower, as clearly shown in the three-dimensional R-curves plotted in Fig. 5.3.

The reason why bone has a lower toughness in shear (mode II) can be understood by examining the direction of the maximum mechanical driving force with crack extension (Fig. 5.4c). As the crack extends, the G_{max} direction remains nearly constant at 74°, *i.e.*, the crack tip remains loaded in shear; thus, the direction of the driving force at the crack tip remains nearly commensurate with the preferred microstructural path. The path that the crack takes, *i.e.*, the deflection angle θ (Fig. 5.4c), is nearly parallel to the preferred microstructural path. Under these conditions, bone will display a low toughness because the crack will have no impediment to following the path of lowest

microstructural resistance since the preferred microstructural and mechanical paths are aligned. There is little motivation for the crack to deflect (with respect to the G_{max} direction), while correspondingly the fracture surfaces are comparatively smooth, which is consistent with the low toughness and shallower R-curves.

The toughness still increases with crack growth in mode II. However, where the preferred mechanical and microstructural paths are aligned, extrinsic toughening in bone results primarily from the formation of (typically at cement lines) microcracks that form ahead and parallel to the main growing crack. The intact regions in between can then act as bridging ligaments, so called "uncracked-ligament" bridging (Figs. 5.4c, 5.5), which can toughen the material by carrying load that would otherwise be used to promote further crack extension. This mechanism, however, is considerably less potent than the crack deflection mechanisms described above [34].

5.3.3. Mixed-mode I-II R-curves

Under mixed-mode loading, prior to crack extension, the direction of the maximum driving force is at an angle between 0° and 74° (depending on the applied mode-mixity) to the original crack plane. As the crack extends, the required driving force for the next increment of crack growth increases (Fig. 5.2b,c), leading to rising R-curve behavior, as in pure mode I and mode II. As might be expected, the competition between the preferred mechanical and microstructural paths results in toughness values that are intermediate between the high mode I values and the low mode II values (Fig. 5.3).

The cause of this behavior is fairly complicated and may likely vary for each sample depending on microstructural variations ahead of the crack tip. However, *in situ* observations in the SEM indicated two different modes of behavior. At one extreme, the deflection angle remained roughly constant, *i.e.*, the crack path followed the preferred microstructural direction (90° deflection), while the path of maximum G diverged from the crack path. Thus, crack deflection here causes significant increases in the toughness with crack growth. As this divergence is never as great as in pure mode I, the R-curves are not as steep. SEM micrographs of the crack path (for Ψ = 13° in Fig. 5.4b) show a combination of toughening mechanisms in the form of crack deflection and uncracked-ligament bridging.

At the other extreme, the direction of the maximum driving force remained constant while the deflection angle changed. In this case, the crack path becomes increasingly dominated by the preferred microstructural direction (see Ψ = 16° in Fig. 5.4b). Again the preferred directions become increasingly divergent with crack extension, although now the salient toughening mechanism appears to be solely crack deflection.

5.4. Discussion

In vivo, bones invariably break under mixed-mode loading with often complicated fracture patterns. The central hypothesis of this work is that the variation in cortical bone toughness with loading mode can be interpreted in terms of the fracture path,

specifically in terms of the competition between the preferred mechanical and microstructural crack paths. The preferred microstructural crack path is along the cement lines, *i.e.*, along the long axis of the bone (Fig. 2.1a), which in the transverse orientation is perpendicular to the original crack plane; the preferred mechanical crack path is the path of the maximum driving force, *i.e.*, the direction of maximum G, which varies between 0° and 74° with respect to the original crack plane for mode I and mode II, respectively [86]. For the toughness of human cortical bone in the transverse orientation (Fig. 2.2b), a consideration of these crack paths clearly shows why bone displays a higher toughness in tension (Mode I) than in shear (Mode II) [104], which at first glance is a surprising result.

In mode I tension, the transverse toughness of human cortical bone increases with crack extension because the preferred mechanical (G_{max}) path remains orthogonal to the preferred microstructural path, which is along the long axis of the bone (Fig. 5.4a). When this occurs, a progressively higher driving force is required for further crack extension, *i.e.*, due to crack deflections in mode I, the toughness of the material increases. This is manifest as the steepest R-curves for any mode-mixity, consistent with the highly deflected crack paths and rough fracture surfaces [104]. Because the bending of bones perpendicular to their long axis would be deemed the most severe form of loading, Nature has clearly designed bone to be most fracture resistant in this orientation.

In mode II (in-plane) shear, the direction of the driving force and the preferred microstructural path are nearly identical (Fig. 5.4c) as the crack propagates. Consequently, the crack is able to nominally follow the preferred microstructural path because the driving force is nearly aligned with this path; deflection is therefore limited and will not be a significant source of toughening. As microcracks now tend to form ahead and parallel to the growing crack, the primary source of toughening is crack bridging, with relatively linear crack paths and planar fracture surfaces (Fig. 5.5). In addition, the R-curves tend to be shallowest in this mode (Fig. 5.3). Clearly, because of this, cortical bone is less resistant to fracture in shear. Cracks can propagate in the shear-like mode that is associated with the linking of nominally parallel microcracks (Fig. 5.5); these shear cracks closely resemble the *en echelon* cracks associated with earthquake faults in rocks [111, 112] (which, like bone, is also a microcracking solid).

Under mixed-mode tension and shear loads, cracks appear to follow a path that leads to an increasing divergence between the preferred mechanical and microstructural paths. However, as this divergence is invariably less than in mode I, R-curves are steeper than in mode II but less so than in mode I. Under these conditions, both primary toughening mechanisms, *i.e.*, crack deflection and uncracked-ligament bridging, prevail.

5.5. Conclusion

Based on an analysis of mixed-mode fracture and crack growth in transversely oriented human cortical bone, the following conclusions can be made.

1. The toughness of bone results from a competition between the direction of the paths of maximum mechanical driving force (G_{max}) and weakest microstructural resistance (along the cement lines parallel to the long axis of the bone). When these directions are commensurate, bone has a low crack-growth toughness; when they are divergent, these fracture toughness values become significantly enhanced.
2. The toughness of bone is highest under pure mode I tensile loading where the preferred microstructural and mechanical paths are most divergent. The competition between these two paths leads to significant crack deflection, which provides the main source of toughening. As the driving force remains coplanar with the original crack after the crack deflects, a larger driving force is required to sustain cracking; R-curves are thus steepest in this loading mode, resulting in the highest crack-growth toughness.
3. The toughness of bone is lowest under pure mode II (in-plane) shear loading where the preferred microstructural and mechanical paths are more closely aligned. Under these conditions, the toughness associated with crack extension is correspondingly much lower and does not increase as significantly with crack extension. Crack paths are thus relatively linear and toughening is associated with crack bridging resulting from the formation of microcracks ahead or parallel to the main growing crack.
4. Under mixed-mode tension and shear loading, the toughness still increases with crack extension due to a progressive divergence of the preferred microstructural and mechanical crack paths. Toughness values are intermediate between those measured in pure mode I and mode II, with toughening associated with both crack deflection and crack bridging.

5.6. Figures

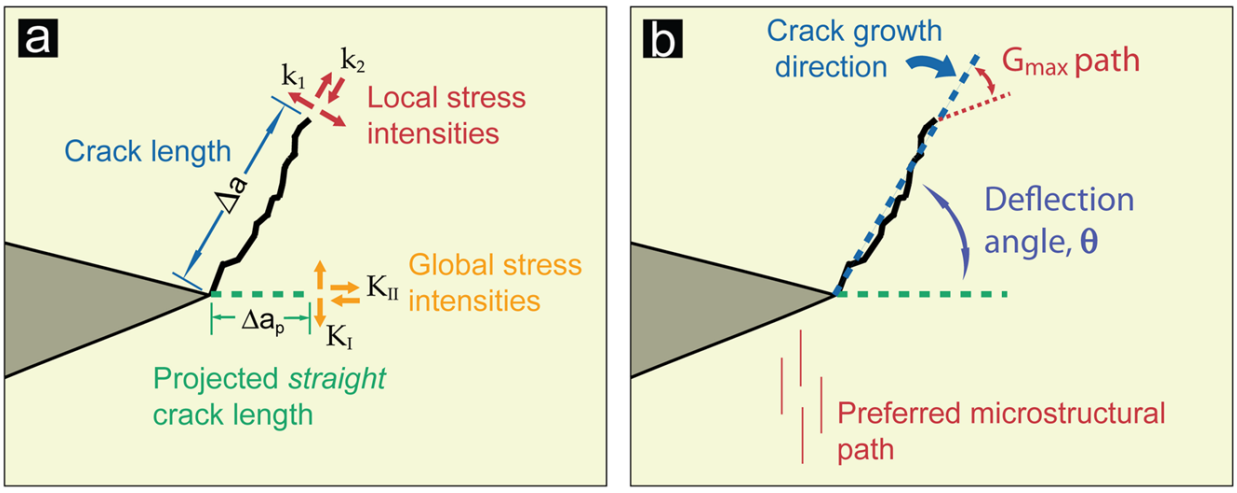

Fig. 5.1 (a) A magnified view of the crack tip shows that when the crack deflects with respect to the original plane of the crack, local stress intensities (k_1 and k_2) arise at the crack tip; the local k's are derived from the global stress intensities (K_I and K_{II}) via a kinked-crack solution. The global stress intensities are calculated with the asymmetric four-point bend solution for a crack with length $a = a_o + \Delta a_p$, which is the length of the kinked crack projected onto the original crack plane. (b) When an asymmetric load is applied, the crack deflects at an angle θ from the original crack plane. The direction of the G_{max} path at each increment of crack growth is assessed from the local stress intensities using the analysis of He and Hutchinson [86].

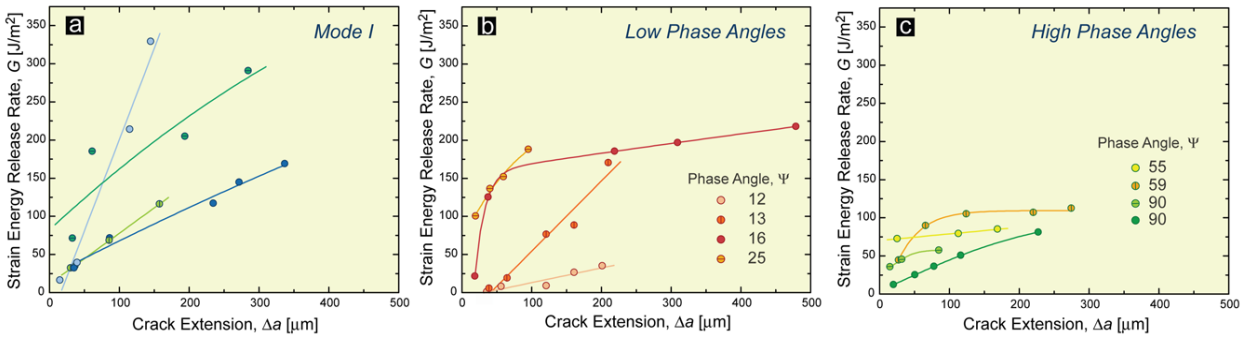

Fig. 5.2 Traditional two-dimensional R-curves for human cortical bone in the transverse orientation loaded in (a) mode I (Ψ = 0°), (b) at low phase angles (Ψ = 12-25°), and (c) at high phase angles (Ψ = 55-90°). The resistance of the material is measured in terms of the strain energy release rate and given as a function of crack extension. As previous R-curves for the tensile opening case have shown, bone exhibits stable crack extension in combined mode I-II loading [34]. The occurrence of a rising R-curve thus indicates that as the crack grows, a larger driving force is needed for crack extension. At higher phase angles, the R-curve is shallower because the paths of maximum mechanical driving force and the preferred microstructural paths (generally along the cement lines) are more closely aligned, which encourages crack deflection along the brittle interfaces in the microstructure.

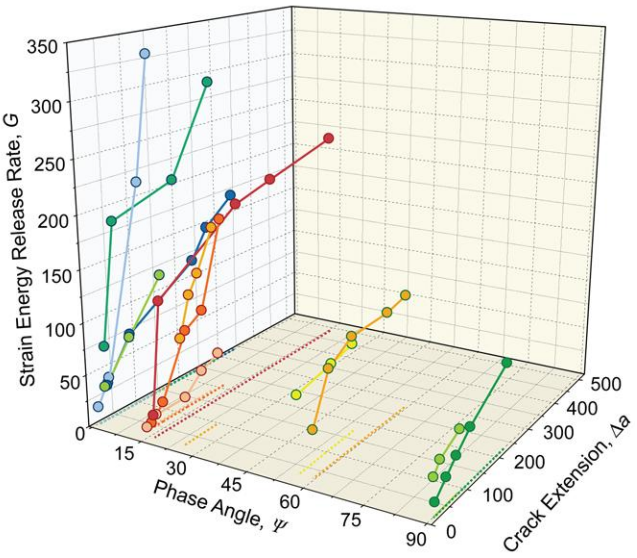

Fig. 5.3 Three-dimensional R-curves for transverse-orientated human cortical bone obtained by plotting the two-dimensional R-curves from Fig. 5.2 together with an additional axis that represents the phase angle, Ψ. The marked decrease in the fracture resistance of the material with crack growth can be seen as the amount of mode II loading (phase angle) increases. The dotted lines are the projections of the three-dimensional lines onto the Ψ-Δ*a* axis.

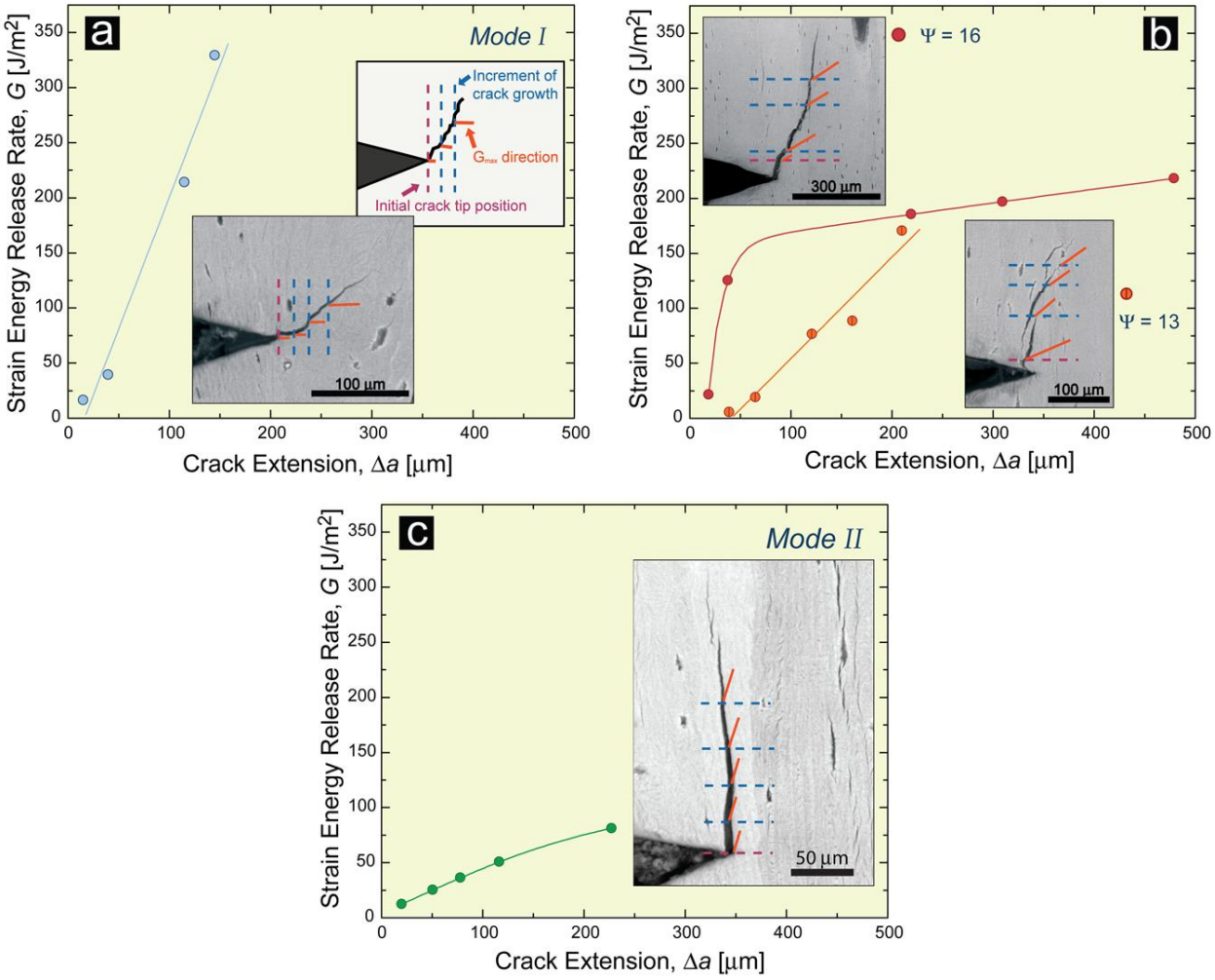

Fig. 5.4 Two-dimensional R-curves for the (a) mode I, (b) mixed-mode, and (c) mode II samples of transverse-orientated human cortical bone along with an image of the crack extension. The dotted red line indicates the initial crack position, the dotted blue lines indicate the increments of crack growth, and the orange lines indicate the G_{max} direction. With respect to the comparison between the G_{max} direction and the actual crack path, higher toughness values result when the driving force is perpendicular to the weak microstructural path.

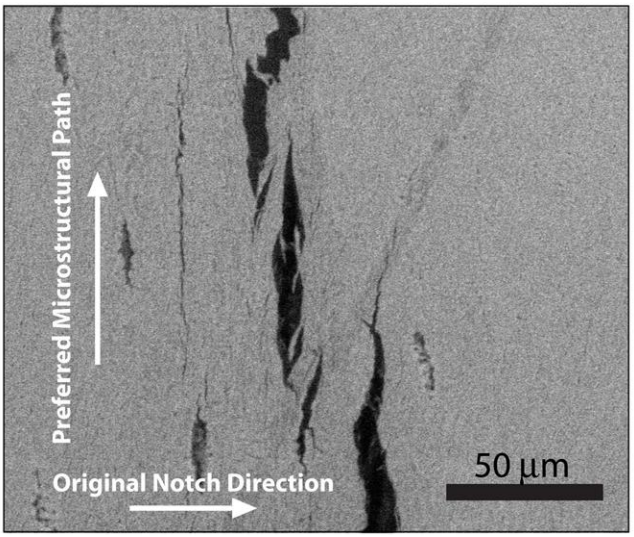

Fig. 5.5 Crack bridging in human cortical bone for a crack loaded in shear (mode II). The crack follows the preferred microstructural path, which is perpendicular to the original plane of the crack. Such apparent shear cracks propagate in a fashion very similar to *en echelon* cracks associated with earthquake faults in microcracking rocks.

Summary and concluding remarks

One key to understanding bone fracture is to discern the deformation and fracture of human cortical bone in terms of its hierarchical, anisotropic structure. This work has shown that the complex structure has significant consequences in terms of bone fracture under physiologically relevant mixed-mode conditions, especially in the transverse orientation where bone is less resistant to shear than tension. Indeed, the relationship between the direction of the mechanical driving force and the direction of the weak microstructural features determines whether the relative toughness in different orientations will be high or low. In addition, this work attempts to provide a framework to explain how biological aging at various structural levels compromises the toughness and strength of cortical bone.

Aging is known to have a negative impact on the mechanical properties of cortical bone. This paper provides a mechanistic framework to describe the fracture of bone from the nanoscale (*i.e.,* the collagen and mineral) to the scale of 10s-100s μm (*i.e.,* osteons) to determine the origin of the deterioration in strength and toughness by linking biological changes at each length-scale (*e.g.,* nonenzymatic crosslinking, osteon density, etc.) to mechanical property measurements (via *in situ* x-ray scattering as well strength and toughness measurements). In particular, the *in situ* x-ray scattering measurements reveal that younger bone is able to deform greater than aged bone; this correlates with an increased amount of nonenzymatic crosslinks in aged bone suggesting that the aged mineralized collagen fibril's capacity to absorb energy is constrained. As is such in aged bone, the additional energy not absorbed by the fibril would need to be absorbed at higher levels of the hierarchy, presumably through microcracking, which is known to be more prevalent in aged bone. As this study shows, aged bone has a higher osteon density leading to smaller crack bridges in the longitudinal orientation and as such a lower toughness compared to young bone. Thus, biological changes in human cortical bone with age lead to a deterioration in mechanical properties with origins at both small and large length-scales.

This study also for the first time provides realistic measurements of the initiation and growth of cracks in human cortical bone under mixed-mode I and II conditions. Indeed, the literature has focused on measuring the mode I toughness of human cortical bone under the presumption that it is the limiting value, as may be the case for most brittle materials. However, this work shows that the toughness in shear is smaller than tension in the transverse orientation. The explanation is that the toughness is always lower when the paths of weakest microstructural resistance and maximum driving force are commensurate (as for the case of shear in the transverse orientation and tension in the longitudinal orientation); this combination will always lead to low crack-growth toughnesses with the main extrinsic toughening mechanism of crack bridging.

When the paths of maximum driving force and weakest microstructural resistance are divergent, the toughness will be high (highest in fact when the directions are perpendicular) and the toughening mechanism of crack deflection will be most active; this case will occur for shear loading in the longitudinal orientation and tensile loading in the transverse orientation. This study in particular reinforces the need to account for the microstructure when measuring the toughness of anisotropic materials. Essentially, fracture needs to be understood when the driving force and the weak microstructural paths are both aligned and misaligned.

These three studies together provide insight into how the fracture toughness is related to the underlying mechanisms in the hierarchical structure. The toughness under mixed-mode conditions relies heavily on which extrinsic crack-tip shielding mechanisms are activated, while the effects of aging have structural consequences on multiple levels that deteriorate the overall toughness and strength.

References

[1] Burr DB. Bone quality: Understanding what matters. J Musculoskelet Neuronal Interact 2004 June;4(2):184-186.

[2] Hui SL, Slemenda CW, Johnston CC. Age and bone mass as predictors of fracture in a prospective-study J Clin Invest 1988 Jun;81(6):1804-1809.

[3] Hazenberg JG, Freeley M, Foran E, Lee TC, Taylor D. Microdamage: A cell transducing mechanism based on ruptured osteocyte processes. J Biomech 2006;39(11):2096-2103.

[4] Canty EG, Kadler KE. Collagen fibril biosynthesis in tendon: a review and recent insights. Comp Biochem Physiol A-Mol Integr Physiol 2002 Dec;133(4):979-985.

[5] Kadler KE, Holmes DF, Trotter JA, Chapman JA. Collagen fibril formation. Biochem J 1996 May;316:1-11.

[6] Ramachandran GN, Kartha G. Structure of collagen. Nature 1955;176(4482):593-595.

[7] Hodge AJ, Petruska JA. Recent studies with the electron microscope on ordered aggregates of the tropocollagen macromolecule. In: Ramachandran GN, editor. Aspects of protein structure. New York: Academic Press, 1963.

[8] Saito M, Marumo K. Collagen cross-links as a determinant of bone quality: a possible explanation for bone fragility in aging, osteoporosis, and diabetes mellitus. Osteoporos Int 2010 Feb;21(2):195-214.

[9] Bailey AJ. Molecular mechanisms of ageing in connective tissues. Mech Ageing Dev 2001 May;122(7):735-755.

[10] Eyre DR, Dickson IR, Vanness K. Collagen cross-linking in human-bone and articular-cartilage - Age-related-changes in the content of mature hydroxypyridinium residues. Biochem J 1988 Jun;252(2):495-500.

[11] Landis WJ, Hodgens KJ, Arena J, Song MJ, McEwen BF. Structural relations between collagen and mineral in bone as determined by high voltage electron microscopic tomography. Microsc Res Tech 1996 Feb;33(2):192-202.

[12] Traub W, Arad T, Weiner S. 3-dimensional ordered distribution of crystals in turkey tendon collagen-fibers. Proc Natl Acad Sci U S A 1989 Dec;86(24):9822-9826.

[13] Weiner S, Traub W. Organization of hydroxyapatite crystals within collagen fibrils FEBS Lett 1986 Oct;206(2):262-266.

[14] Arsenault AL. Image-analysis of collagen-associated mineral distribution in cryogenically prepared turkey leg tendons. Calcif Tissue Int 1991 Jan;48(1):56-62.

[15] Landis WJ, Hodgens KJ, Song MJ, Arena J, Kiyonaga S, Marko M, et al. Mineralization of collagen may occur on fibril surfaces: Evidence from conventional and high-voltage electron microscopy and three-dimensional imaging. J Struct Biol 1996 Jul-Aug;117(1):24-35.

[16] Maitland ME, Arsenault AL. A correlation between the distribution of biological apatite and amino-acid sequence of type-I collagen Calcif Tissue Int 1991 May;48(5):341-352.

[17] Saito M, Marumo K, Fujii K, Ishioka N. Single-column high-performance liquid chromatographic-fluorescence detection of immature, mature, and senescent cross-links of collagen. Anal Biochem 1997;253(1):26-32.

[18] Martin RB, Burr DB. Structure, Function, and Adaptation of Compact Bone. New York: Raven Press, 1989.

[19] Wagermaier W, Gupta HS, Gourrier A, Burghammer M, Roschger P, Fratzl P. Spiral twisting of fiber orientation inside bone lamellae. Biointerphases 2006 Mar;1(1):1-5.

[20] Weiner S, Wagner HD. The material bone: Structure mechanical function relations. Annu Rev Mater Sci 1998;28:271-298.

[21] Skedros JG, Holmes JL, Vajda EG, Bloebaum RD. Cement lines of secondary osteons in human bone are not mineral-deficient: New data in a historical perspective. Anat Rec A 2005;286A:781-803.

[22] Currey JD. Bones: structure and mechanics. Second edition: Princeton University Press, 2002.

[23] Schaffler MB, Burr DB, Frederickson RG. Morphology of the osteonal cement line in human bone. Anat Rec 1987;217:223-228.

[24] McKee MD, Nanci A. Osteopontin at mineralized tissue interfaces in bone, teeth, and osseointegrated implants: Ultrastructural distribution and implications for mineralized tissue formation, turnover, and repair. Microsc Res Tech 1996 Feb;33(2):141-164.

[25] Fantner GE, Adams J, Turner P, Thurner PJ, Fisher LW, Hansma PK. Nanoscale ion mediated networks in bone: Osteopontin can repeatedly dissipate large amounts of energy. Nano Lett 2007 Aug;7(8):2491-2498.

[26] Hunter GK, Kyle CL, Goldberg HA. Modulation of crystal formation by bone phosphoproteins - structural specificity of the osteopontin-mediated inhibition of hydroxyapatite formation. Biochem J 1994 Jun;300:723-728.

[27] McCalden RW, McGeough JA, Barker MB, Courtbrown CM. Age-related-changes in the tensile properties of cortical bone - the relative importance of changes in porosity, mineralization, and microstructure. J Bone Joint Surg-Am Vol 1993 Aug;75A(8):1193-1205.

[28] Nalla RK, Kinney JH, Ritchie RO. Mechanistic fracture criteria for the failure of human cortical bone. Nat Mater 2003;2(3):164-168.

[29] Zioupos P, Currey JD. Changes in the Stiffness, Strength, and Toughness of Human Cortical Bone With Age. Bone 1998;22(1):57-66.

[30] Brown CU, Yeni YN, Norman TL. Fracture toughness is dependent on bone location—A study of the femoral neck, femoral shaft, and the tibial shaft. J Biomed Mater Res 2000;49(3):380-389.

[31] Norman TL, Vashishth D, Burr DB. Fracture toughness of human bone under tension. J Biomech 1995;28(3):309-320.

[32] Wang X, Shen X, Li X, Agrawal CM. Age-related changes in the collagen network and toughness of bone. Bone 2002 Jul;31(1):1-7.

[33] ASTM E 1820-09. Annual Book of ASTM Standards. Standard Test Method for Measurement of Fracture Toughness. West Conshohocken, Pennsylvania, USA: ASTM International, 2010.

[34] Koester KJ, Ager JW, Ritchie RO. The true toughness of human cortical bone measured with realistically short cracks. Nat Mater 2008;7(8):672-677.

[35] Launey ME, Chen PY, McKittrick J, Ritchie RO. Mechanistic aspects of the fracture toughness of elk antler bone. Acta Biomaterialia 2010;6(4):1505-1514.

[36] Nalla RK, Kruzic JJ, Kinney JH, Ritchie RO. Effect of aging on the toughness of human cortical bone: evaluation by R-curves. Bone 2004 Dec;35(6):1240-1246.

[37] Vashishth D. Rising crack-growth-resistance behavior in cortical bone:: implications for toughness measurements. J Biomech 2004;37(6):943-946.

[38] Ritchie RO. Mechanisms of fatigue crack-propagation in metals, ceramics and composites - role of crack tip shielding. Mater Sci Eng A-Struct Mater Prop Microstruct Process 1988 Aug;103(1):15-28.

[39] Ritchie RO. Mechanisms of fatigue-crack propagation in ductile and brittle solids. Int J Fract 1999;100(1):55-83.

[40] Launey ME, Buehler MJ, Ritchie RO. On the mechanistic origins of toughness in bone. Annual Review of Materials Research, Vol 40, 2010. p. 25-53.

[41] Zhang ZQ, Zhang YW, Gao HJ. On optimal hierarchy of load-bearing biological materials. Proc R Soc B-Biol Sci 2011 Feb;278(1705):519-525.

[42] Buehler MJ, Wong SY. Entropic elasticity controls nanomechanics of single tropocollagen molecules. Biophys J 2007 Jul;93(1):37-43.

[43] Gautieri A, Buehler MJ, Redaelli A. Deformation rate controls elasticity and unfolding pathway of single tropocollagen molecules. J Mech Behav Biomed Mater 2009 Apr;2(2):130-137.

[44] Gao HJ, Ji BH, Jager IL, Arzt E, Fratzl P. Materials become insensitive to flaws at nanoscale: Lessons from nature. Proc Natl Acad Sci U S A 2003 May;100(10):5597-5600.

[45] Jäger I, Fratzl P. Mineralized collagen fibrils: A mechanical model with a staggered arrangement of mineral particles. Biophys J 2000;79(4):1737-1746.

[46] Gupta HS, Seto J, Wagermaier W, Zaslansky P, Boesecke P, Fratzl P. Cooperative deformation of mineral and collagen in bone at the nanoscale. Proc Natl Acad Sci U S A 2006 Nov;103(47):17741-17746.

[47] Ji B, Gao H. Mechanical properties of nanostructure of biological materials. J Mech Phys Solids 2004;52(9):1963-1990.

[48] Ji BH. An atomistic study of the strength of protein-mineral interface of biological materials with a biomimicking model system at nanoscale. J Comput Theor Nanosci 2010 Jul;7(7):1265-1271.

[49] Ji BH, Gao HJ. Mechanical principles of biological nanocomposites. Annual Review of Materials Research, Vol 40. Palo Alto: Annual Reviews, 2010. p. 77-100.

[50] Siegmund T, Allen MR, Burr DB. Failure of mineralized collagen fibrils: Modeling the role of collagen cross-linking. J Biomech 2008;41(7):1427-1435.

[51] Vashishth D, Gibson GJ, Khoury JI, Schaffler MB, Kimura J, Fyhrie DP. Influence of nonenzymatic glycation on biomechanical properties of cortical bone. Bone 2001;28(2):195-201.

[52] Fantner GE, Hassenkam T, Kindt JH, Weaver JC, Birkedal H, Pechenik L, et al. Sacrificial bonds and hidden length dissipate energy as mineralized fibrils separate during bone fracture. Nat Mater 2005;4(8):612-616.

[53] Thompson JB, Kindt JH, Drake B, Hansma HG, Morse DE, Hansma PK. Bone indentation recovery time correlates with bond reforming time. Nature 2001 Dec;414(6865):773-776.

[54] Krauss S, Fratzl P, Seto J, Currey JD, Estevez JA, Funari SS, et al. Inhomogeneous fibril stretching in antler starts after macroscopic yielding: Indication for a nanoscale toughening mechanism. Bone 2009;44(6):1105-1110.

[55] Gupta HS, Wagermaier W, Zickler GA, Hartmann J, Funari SS, Roschger P, et al. Fibrillar level fracture in bone beyond the yield point. Int J Fract 2006 Jun;139(3-4):425-436.

[56] Harrington MJ, Gupta HS, Fratzl P, Waite JH. Collagen insulated from tensile damage by domains that unfold reversibly: In situ X-ray investigation of mechanical yield and damage repair in the mussel byssus. J Struct Biol 2009;167(1):47-54.

[57] Bailey AJ, Sims TJ, Avery NC, Miles CA. Chemistry of collagen cross-links - glucose-mediated covalent cross-linking of type-IV collagen in lens capsules. Biochem J 1993 Dec;296:489-496.

[58] Nalla RK, Kruzic JJ, Ritchie RO. On the origin of the toughness of mineralized tissue: microcracking or crack bridging? Bone 2004 May;34(5):790-798.

[59] Nalla RK, Kruzic JJ, Kinney JH, Ritchie RO. Mechanistic aspects of fracture and R-curve behavior in human cortical bone. Biomaterials 2005;26(2):217-231.

[60] Bilby BA, Cardew GE, Howard IC. Stress intensity factors at the tips of kinked and forked cracks. In: Taplin DMR, editor. Fourth International Conference on Fracture; 1977 1978

19-24 June; Waterloo, Ont., Canada: Pergamon; 1977. p. 197-200.

[61] Wasserman N, Brydges B, Searles S, Akkus O. In vivo linear microcracks of human femoral cortical bone remain parallel to osteons during aging. Bone 2008 Nov;43(5):856-861.

[62] Nalla R, Kruzic J, Kinney J, Balooch M, Ager III J, Ritchie R. Role of microstructure in the aging-related deterioration of the toughness of human cortical bone. Mater Sci Eng, C 2006;26:1251-1260.

[63] Sell DR, Monnier VM. Structure elucidation of a senescence cross-link from human extracellular matrix. Implication of pentoses in the aging process. J Biol Chem 1989 December 25, 1989;264(36):21597-21602.

[64] Odetti P, Rossi S, Monacelli F, Poggi A, Cirnigliaro F, Federici M, et al. Advanced glycation end-products and bone loss during aging. Ann NY Acad Sci 2005;1043(1):710-717.

[65] Ager JW, Balooch G, Ritchie RO. Fracture, aging, and disease in bone. J Mater Res 2006 Aug;21(8):1878-1892.

[66] Garnero P, Borel O, Gineyts E, Duboeuf F, Solberg H, Bouxsein ML, et al. Extracellular post-translational modifications of collagen are major determinants of biomechanical properties of fetal bovine cortical bone. Bone 2006;38(3):300-309.

[67] ASTM D790-10. Annual Book of ASTM Standards. Standard test methods for flexural properties of unreinforced and reinforced plastics and electrical insulating materials. West Conshohocken, Pennsylvania, USA: ASTM International, 2010.

[68] Barth HD, Launey ME, MacDowell AA, Ager JW, Ritchie RO. On the effect of X-ray irradiation on the deformation and fracture behavior of human cortical bone. Bone 2010 Jun;46(6):1475-1485.

[69] Kinney JH, Nichols MC. X-ray tomographic microscopy (Xtm) using synchrotron radiation. Annu Rev Mater Sci 1992;22:121-152.

[70] Vlassenbroeck J, Dierick M, Masschaele B, Cnudde V, Hoorebeke L, Jacobs P. Software tools for quantification of X-ray microtomography. Nucl Instrum Methods Phys Res Sect A-Accel Spectrom Dect Assoc Equip 2007 Sep;580(1):442-445.

[71] Mercury CS. Avizo™ 3D Visualization Framework. Chelmsford, MA.

[72] Tang SY, Zeenath U, Vashishth D. Effects of non-enzymatic glycation on cancellous bone fragility. Bone 2007;40(4):1144-1151.

[73] Woessner JF. The determination of hydroxyproline in tissue and protein samples containing small proportions of this imino acid. Arch Biochem Biophys 1961;93(2):440-447.

[74] Busse B, Hahn M, Schinke T, Püschel K, Duda GN, Amling M. Reorganization of the femoral cortex due to age-, sex-, and endoprosthetic-related effects emphasized by osteonal dimensions and remodeling. J Biomed Mater Res, Part A 2010;92A(4):1440-1451.

[75] Ritchie RO, Buehler MJ, Hansma P. Plasticity and toughness in bone. Phys Today 2009 Jun;62(6):41-47.

[76] Ager JW, Nalla RK, Balooch G, Kim G, Pugach M, Habelitz S, et al. On the increasing fragility of human teeth with age: a deep-UV resonance Raman study. J Bone Miner Res 2006;21(12):1879-1887.

[77] Mikhonin AV, Ahmed Z, Ianoul A, Asher SA. Assignments and conformational dependencies of the amide III peptide backbone UV resonance Raman bands. J Phys Chem B 2004 Dec;108(49):19020-19028.

[78] Tang SY, Vashishth D. Non-enzymatic glycation alters microdamage formation in human cancellous bone. Bone 2010;46(1):148-154.

[79] Mori S, Harruff R, Ambrosius W, Burr DB. Trabecular bone volume and microdamage accumulation in the femoral heads of women with and without femoral neck fractures. Bone 1997;21(6):521-526.

[80] Schaffler MB, Choi K, Milgrom C. Aging and matrix microdamage accumulation in human compact bone. Bone 1995;17(6):521-525.

[81] Irwin GR. Analysis of stresses and strains near the end of a crack traversing a plate. J Appl Mech 1957;24:361-364.

[82] Qian J, Fatemi A. Mixed mode fatigue crack growth: A literature survey. Eng Fract Mech 1996;55(6):969-990.

[83] Singh D, Shetty DK. Fracture toughness of polycrystalline ceramics in combined mode I and mode II loading. J Am Ceram Soc 1989;72(1):78-84.

[84] Suresh S, Shih CF, Morrone A, O'Dowd NP. Mixed-mode fracture toughness of ceramic materials. J Am Ceram Soc 1990;73(5):1257-1267.

[85] Melin S. When does a crack grow under mode II conditions? Int J Fract 1986;30(2):103-114.

[86] He M-Y, Hutchinson JW. Kinking of a crack out of an interface. J Appl Mech 1989;56:270-278.

[87] Wang J-S. Interfacial fracture toughness of a copper/alumina system and the effect of the loading phase angle. Mech Mater 1995;20(3):251-259.

[88] Evans AG, Hutchinson JW. Effects of non-planarity on the mixed mode fracture resistance of bimaterial interfaces. Acta Metall 1989;37(3):909-916.

[89] He MY, Cao HC, Evans AG. Mixed-mode fracture: The four-point shear specimen. Acta Metall Mater 1990;38(5):839-846.

[90] Ritchie RO, Cannon RM, Dalgleish BJ, Dauskardt RH, McNaney JM. Mechanics and mechanisms of crack growth at or near ceramic-metal interfaces: interface engineering strategies for promoting toughness. Mater Sci Eng A 1993;166(1-2):221-235.

[91] Norman TL, Nivargikar SV, Burr DB. Resistance to crack growth in human cortical bone is greater in shear than in tension. J Biomech 1996;29(8):1023-1031.

[92] Feng Z, Rho J, Han S, Ziv I. Orientation and loading condition dependence of fracture toughness in cortical bone. Mater Sci Eng C 2000;11(1):41-46.

[93] He M, Hutchinson JW. Asymmetric four-point crack specimen. J Appl Mech 2000;67(1):207-209.

[94] Tada H, Paris PC, Irwin GR. The Stress Analysis of Cracks Handbook. St. Louis, MO: Del Research Corp., 1985.

[95] Anderson TL. Fracture Mechanics: Fundamentals and Applications. 2nd ed. Boca Raton: CRC Press, 1995.

[96] Jen WK, Lin HC, Hua K. Calculation of stress intensity factors for combined mode bend specimens. In: Taplin DMR, editor. Fracture 1977: Advances in Research on the Stress and Fracture of Materials/Fourth International Conference on Fracture: Pergamon Press, 1977. p. 123-133.

[97] Jernkvist LO. Fracture of wood under mixed mode loading: II. Experimental investigation of Picea abies. Eng Fract Mech 2001;68(5):565-576.

[98] Li M, Sakai M. Mixed-mode fracture of ceramics in asymmetric four-point bending: Effect of crack-face grain interlocking/bridging. J Am Ceram Soc 1996;79(10):2718-2726.

[99] Fratzl P, Weinkamer R. Nature's hierarchical materials. Prog Mater Sci 2007 Nov;52(8):1263-1334.

[100] Yeni YN, Norman TL. Calculation of porosity and osteonal cement line effects on the effective fracture toughness of cortical bone in longitudinal crack growth. J Biomed Mater Res 2000 Sep;51(3):504-509.

[101] Peterlik H, Roschger P, Klaushofer K, Fratzl P. From brittle to ductile fracture of bone. Nat Mater 2006 Jan;5(1):52-55.

[102] Yeni YN, Fyhrie DP. A rate-dependent microcrack-bridging model that can explain the strain rate dependency of cortical bone apparent yield strength. J Biomech 2003 Sep;36(9):1343-1353.

[103] Nalla RK, Stolken JS, Kinney JH, Ritchie RO. Fracture in human cortical bone: local fracture criteria and toughening mechanisms. J Biomech 2005 Jul;38(7):1517-1525.

[104] Zimmermann EA, Launey ME, Barth HD, Ritchie RO. Mixed-mode fracture of human cortical bone. Biomaterials 2009;30(29):5877-5884.

[105] Kitagawa H, Yuuki R, Ohira T. Crack-morphological aspects in fracture mechanics. Eng Fract Mech 1975 September;7(3):515-529.

[106] Cotterell B, Rice JR. Slightly curved or kinked cracks. Int J Fract 1980;16(2):155-169.

[107] Lo KK. Analysis of branched cracks J Appl Mech-Trans ASME 1978;45(4):797-802.

[108] Karihaloo BL, Keer LM, Nematnasser S. Crack kinking under nonsymmetric loading. Eng Fract Mech 1980;13(4):879-888.

[109] Chatterjee SN. The stress field in the neighbourhood of a branched crack in an infinite elastic sheet. Int J Solids Struct 1975 May;11(5):521-538.

[110] He MY, Hutchinson JW. Kinking of a crack out of an interface: Tabulated solution coefficients. Cambridge, MA: Harvard University Report MECH-113A; 1989. Report No.: MECH-113A.

[111] Peng S, Johnson AM. Crack growth and faulting in cylindrical specimens of chelmsford granite. Int J Rock Mech Min Sci 1972;9(1):37-&.

[112] Etchecopar A, Granier T, Larroque JM. Origin of en echelon cracks - propagation of faults. CR Acad Sci II C 1986 Feb;302(7):479-484.